Nanoscale



REVIEW

View Article Online
View Journal | View Issue



Cite this: Nanoscale, 2021, 13, 10239

Ab initio nonadiabatic molecular dynamics of charge carriers in metal halide perovskites

Wei Li, *\omega *a Yalan She, *a Andrey S. Vasenko *\omega b,c and Oleg V. Prezhdo *\omega *a

Photoinduced nonequilibrium processes in nanoscale materials play key roles in photovoltaic and photocatalytic applications. This review summarizes recent theoretical investigations of excited state dynamics in metal halide perovskites (MHPs), carried out using a state-of-the-art methodology combining nonadiabatic molecular dynamics with real-time time-dependent density functional theory. The simulations allow one to study evolution of charge carriers at the ab initio level and in the time-domain, in direct connection with time-resolved spectroscopy experiments. Eliminating the need for the common approximations, such as harmonic phonons, a choice of the reaction coordinate, weak electron-phonon coupling, a particular kinetic mechanism, and perturbative calculation of rate constants, we model full-dimensional quantum dynamics of electrons coupled to semiclassical vibrations. We study realistic aspects of material composition and structure and their influence on various nonequilibrium processes, including nonradiative trapping and relaxation of charge carriers, hot carrier cooling and luminescence, Auger-type charge-charge scattering, multiple excitons generation and recombination, charge and energy transfer between donor and acceptor materials, and charge recombination inside individual materials and across donor/acceptor interfaces. These phenomena are illustrated with representative materials and interfaces. Focus is placed on response to external perturbations, formation of point defects and their passivation, mixed stoichiometries, dopants, grain boundaries, and interfaces of MHPs with charge transport layers, and quantum confinement. In addition to bulk materials, perovskite quantum dots and 2D perovskites with different layer and spacer cation structures, edge passivation, and dielectric screening are discussed. The atomistic insights into excited state dynamics under realistic conditions provide the fundamental understanding needed for design of advanced solar energy and optoelectronic devices.

Received 30th March 2021, Accepted 14th May 2021 DOI: 10.1039/d1nr01990b

rsc.li/nanoscale

1 Introduction

Solar cells based on metal-halide perovskites (MHPs) have been attracting intense attention because of their low cost and high power conversion efficiency (PCE) that evolved rapidly from 3.5% to 25.2% over the past decade. The champion efficiency of perovskite solar cells (PSCs), 25.2%, is comparable to those of commercially available solar cell technologies, such as 26.3% for crystalline silicon and 23.3% for copper indium gallium selenide solar cells. It is now commonly recognized that the superior performance of PSCs originates from remarkable optoelectronic properties, including small exciton binding energies, high absorption coefficients, large carrier

Nonradiative charge recombination is very common in solar cells due to the presence of several recombination channels, such as bimolecular recombination, trap-assisted recombination, and both phonon and Auger mechanisms of energy losses. Nonradiative recombination dissipates electronic energy to heat, lowers density of photogenerated carriers, and limits open circuit voltage, constituting the major pathways for efficiency losses in photovoltaic devices. By contrast, radiative recombination leads to emission of photons, *i.e.*, lumine-

lifetime and diffusion lengths, and inexpensive fabrication cost, ^{4,5} which have been linked with unusual properties combining features of inorganic, organic and even liquid matter, and leading to atypical defect physics, ⁶ direct-to-indirect band gap transitions, ⁷ polaron screening, ^{8,9} ferroelectric domains, ^{10,11} Rashba splitting, ¹² *etc.* Nevertheless, the optimal PCE of PSCs is still below the radiative efficiency limit according to the Shockley–Queisser theory, which reaches 33.7% at the band gap of 1.34 eV. ¹³ Fundamental understanding of the photo-physics and excited-state properties, in addition to material development and device optimization, could pave the way for further improvement of PSC performance.

^aSchool of Chemistry and Materials Science, Hunan Agricultural University, Changsha 410128, People's Republic of China. E-mail: weili@hunau.edu.cn
^bHSE University. 101000 Moscow. Russia

^cI.E. Tamm Department of Theoretical Physics, P.N. Lebedev Physical Institute, Russian Academy of Sciences, 119991 Moscow, Russia

^dDepartment of Chemistry, University of Southern California, Los Angeles, California90089, USA. E-mail: prezhdo@usc.edu

scence. Luminescence quantum yield would reach unity if nonradiative recombination were negligible. For PSCs, nonradiative recombination dominates radiative recombination, since the early reports demonstrated that emission quantum efficiencies in state-of-the-art devices were relatively low.¹⁴ To further improve PSCs performance towards the Shockley-Queisser efficiency limit, it is imperative to eliminate all possible nonradiative recombination pathways. Numerous strategies have been devoted to this topic, including chemical surface treatment, 15 compositional engineering, 16 exposure to environmental factors such as oxygen, moisture, and light, 17 reduction of dimensionality, 18 variations in temperature, pressure, and electric field, 19-21 and ferroelectric polarization tuning. 10 Many types of time-resolved ultrafast spectroscopies, including photoluminescence (PL), terahertz (THz), and transient absorption (TA) measurements, have been utilized to study evolution of charge carriers, exemplifying these realistic factors in PSCs and providing huge amounts of data that are typically interpreted phenomenologically. The mechanisms responsible for carrier relaxation and energy flow under realistic conditions are only partially established and often remain controversial.

Nonadiabatic molecular dynamics (NA-MD) modelling can generate fundamental insights into the coupled electron-nuclei dynamics at the atomistic level, complementing massive experimental spectroscopic investigations. The NA-MD methodology is nontrivial and requires both input from accurate electronic structure calculations and sophisticated algorithms for evolving quantum mechanical electrons coupled to classical or semiclassical nuclei. Many of the existing methodologies are exceedingly expensive for application to MHPs. Time-domain density functional theory (TD-DFT) provides a rigorous and efficient atomistic description of structural and electronic properties of MHPs, explicitly considering their time evolution, from the ab initio level of theory. Ab initio NA-MD has been widely used to simulate nonradiative trapping and relaxation, charge and energy transfer, photochemical reactions, and other nonequilibrium processes in a broad range of molecular, condensed matter, and nanoscale systems, providing structure-property relationships and design principles for creating better materials.^{22–26}

This review focuses on application of the TD-DFT/NA-MD methodology, as developed in our group²⁷ and by others, ^{28–32} to MHPs. It highlights how TD-DFT/NA-MD can be used to provide fundamental understanding of excited state processes in MHPs, in direct connection with experiments. The ab initio atomistic description of the photo-induced charge carrier dynamics, as they occur in nature, establish detailed mechanisms of charge and energy flow, identify the key roles played by electron-vibrational and electron-electron interactions, and generate guidelines for further improvement of performance of PSCs and related devices.

This review discusses only representative works dedicated to theoretical understanding of the excited state dynamics in PSCs, and there are many related studies that are not mentioned here. Readers are referred to other reviews for comprehensive accounts of different topics in PSCs. 33-40 The structure of the current review is as follows: section 2 outlines methodological aspects of NA-MD and TD-DFT. Section 3 exemplifies modeling of charge recombination dynamics of perovskites under external stimuli, such varying temperature, pressure and electric fields. Section 4 illustrates simulations of nonradiative trapping and relaxation process in perovskites containing defects. The unusual defect properties of PSCs are highlighted. Section 5 is devoted to discussion of photoexcitation dynamics in 2D layered perovskites. Section 6 discusses hot carrier cooling in low-dimensional perovskites. The last Section provides an outlook of the field.

2 Simulation methodology

The following subsections provide an introduction into NA-MD and TD-DFT in the Kohn-Sham (KS) representation.

2.1 Nonadiabatic molecular dynamics

NA-MD describes the evolution of a coupled electron-nuclear system involving transition between different electronic states. Motion of classical nuclei drives quantum mechanical evolution of electrons, in turn, influences classical nuclear



Wei Li

Wei Li completed his PhD in Physical Chemistry with Prof. Hong-Xing Zhang at Institute of Theoretical Chemistry of Jilin University in 2017. In 2014, he visited Prof. Oleg Prezhdo's group at University of Southern California. Since 2018, he is a professor of Chemistry at Hunan Agricultural University. current research interests focus on photoexcitation dynamics in nanoscale solar energy materials.



Yalan She

Yalan She is a graduate student in the School of Chemistry and Materials Science at Hunan Agricultural University under the supervision of Prof. Wei Li since 2020. Her research mainly focus on the photoexcitation dynamics in lead-free double perovskites.

dynamics. There exist several mixed quantum-classical approaches for modeling coupled electronic-nuclear dynamics. In Ehrenfest dynamics, 41-43 also known as the mean-field approximation, classical nuclei are propagated along the potential energy surface that is an average over currently occupied electronic states. Correlations of nuclear motions to different electronic states are captured by surface hopping approaches. Recent reviews give a detailed description of various NA-MD methods.44-47

2.2 Fewest switches surface hopping

Tully's fewest switches surface hopping (FSSH)⁴⁸ is by far the most popular NA-MD algorithm due to its robustness and computational simplicity. FSSH prescribes a probability of hopping between electronic states based on solution of the time-dependent Schrodinger equation (TD-SE). If the TD-SE is solved in the adiabatic basis, with c_i representing the quantum mechanical amplitude for state i, then the FSSH probability is given by:

$$g_{jk}(t, \Delta t) = \max\left(0, \frac{b_{jk}\Delta t}{a_{\text{mm}}(t)}\right)$$
 (1)

$$b_{jk} = -2\text{Re}(a_{jk}^* d_{jk} \cdot \dot{R}); \quad a_{jk} = c_j c_k^*$$
 (2)

Here, $g_{jk}(t,\Delta t)$ is the hopping probability between states j and k within a sufficiently small time interval Δt . $d_{ik} \cdot \dot{R}$ is the nonadiabatic coupling (NAC), as we will introduce below. To determine whether the system should hop to a new state or remain in the current state, hopping probability is compared to a uniformly distributed random number. This feature ensures the correct probability flux from one state to another. Velocity adjustment is made in the direction of the NAC vector to conserve the total energy during a hop. Hop will be rejected if there is inadequate energy for velocity rescaling. The hoprejection rule creates detailed balance between upward and

downward transitions. The FSSH algorithm can be simplified by replacing the velocity rescaling and hop rejection with multiplication of the hopping probability with the Boltzmann factor for transitions upward in energy, or the Fermi-Dirac distribution factor, if ensembles of electrons are considered.⁴⁹ The replacement is valid if the distribution of energy within vibrational modes is Boltzmann at the time of the transition. This simplification leads to significant computational savings, and then a ground state nuclear trajectory in place of multiple excited state trajectories can be used directly. This technique is often referred to as the classical path approximation (CPA) or neglect of back reaction approximation (NBRA).50

A notable generalization of the FSSH algorithm, to include many-particle transitions and super-exchange processes, is provided by global flux surface hopping (GFSH).⁵¹

2.3 Decoherence-induced surface hopping

One long-recognized shortcoming of the Ehrenfest method, the standard FSSH algorithm, and other NA-MD approaches is the issue of over-coherence among electronic amplitudes. 52,53 The physical origin of this deficiency is that NA-MD treats nuclei classically and neglects quantum aspects of electronnuclear coupling. From a theoretical viewpoint, decoherence is defined via the reduced density matrix, whose off-diagonal elements describe the coherences. Solution of the TD-SE for electrons, subject to the classical field of nuclei, does not represent decay of off-diagonal elements of the reduced electronic density matrix, as it happens in a fully quantum electronnuclear calculation. Neglect of decoherence typically leads to faster transitions. Decoherence effects are important when the decoherence time is significantly shorter than the transition time. The quantum Zeno effect illustrates the strong influence of decoherence on quantum transitions.⁵⁴ Decoherence can be ignored if the relaxation process occurs rapidly by successive hops within a dense manifold of states of valence and conduction bands in systems such as carbon nanotubes,55,56



Andrey S. Vasenko

Andrey Vasenko is a theoretical physicist who studies quantum phenomena in nanostructures, author of over 40 articles in leading peer-reviewed journals. Since 2015, he is a professor at the HSE University in Moscow. In 2002, he graduated with honors from Moscow State University. He holds a habilitated doctorate degree from the Grenoble Alpes University (France) and a PhD degree from Chalmers University (Sweden).



Oleg V. Prezhdo

Oleg Prezhdo studied Theoretical Chemistry in Kharkiv University, Ukraine. He completed PhD with Peter Rossky at UT-Austin. After a 1-year postdoc with John Tully at Yale, he joined University of Washington in 1998, achieving Associate and Full Professor in 2002 and 2005. In 2010 he moved to University of Rochester, and in 2014 to University of Southern California, where he is Professor of Chemistry, Physics, Astronomy, and Chemical

Engineering. Recipient of multiple awards, he is Executive Editor for Journal of Physical Chemistry Letters and has h-index of 77. He studies quantum dynamics in nanoscale, condensed matter, molecular and biological systems.

graphene,⁵⁷ and quantum dots.⁵⁸ Then, the FSSH algorithm can be used directly. A number of groups have been working on fixing the overcoherence issue of FSSH. 52,59-69 Introduction of decoherence by means of a stochastic wave-function collapse⁴² provides the physical mechanism for surface hopping, as implemented in the decoherence-induced surface hopping (DISH) approach.⁵⁹ DISH provides a unified description of decoherence and NA transitions, extending the quantum-classical simulations to large quantum systems in macroscopic environments.

Time-domain density functional theory

The coupled electron-nuclei dynamics can be characterized in TD-DFT by time-dependent single-electron KS orbitals, $\varphi_{\rm p}(r, R, R)$ t), whose evolution is determined by the TD-KS:

$$i\hbar\frac{\partial\varphi_{\rm p}(r,R,t)}{\partial t}=H(r,R,t)\varphi_{\rm p}(r,R,t) \eqno(3)$$

Expanding $\varphi_p(r, R, t)$ in the adiabatic basis $\tilde{\varphi}_p(r, R(t))$,

$$\varphi_{\rm p}(r,R,t) = \sum_{k=1}^{N_{\rm e}} c_{\rm pk}(t) \Big| \tilde{\varphi}_{\rm p}(r,R(t)) \Big\rangle \tag{4}$$

inserting eqn (4) to eqn (3) and projecting both sides of the resulting equation onto the adiabatic orbital basis yields the following equations-of-motion (EOM) for the time-dependent expansion coefficients:

$$i\hbar \frac{\partial c_{\rm pk}(t)}{\partial t} = \sum_{m=1}^{N_{\rm c}} c_{\rm pm}(t) (\varepsilon_{\rm m} \delta_{\rm km} - d_{\rm km} \cdot \dot{R})$$
 (5)

Here, ε_{m} is the eigenvalue of the adiabatic basis. The last term in eqn (5) is the NAC:

$$d_{\rm km} \cdot \dot{R} = \langle \tilde{\varphi}_{\rm k}(r, R(t)) | \nabla_{\rm R} | \tilde{\varphi}_{\rm m}(r, R(t)) \rangle \cdot \dot{R}$$
 (6)

The first term of the RHS of eqn (6) characterizes sensitivity of adiabatic KS orbitals to nuclear motions, and the second term is the corresponding nuclear velocity. In order to avoid the expensive gradient calculation in the first term of the RHS in eqn (6), the following 2-point numerical differentiation according to Hammes-Schiffer and Tully⁷⁰ is used:

$$\begin{split} &\langle \tilde{\varphi}_{\mathbf{k}}(r,R(t)) | \nabla_{\mathbf{R}} | \tilde{\varphi}_{\mathbf{m}}(r,R(t)) \rangle \cdot \dot{R} = \left\langle \tilde{\varphi}_{\mathbf{k}}(r,R(t)) | \frac{\partial \tilde{\varphi}_{\mathbf{m}}(r,R(t))}{\vartheta t} \right\rangle \\ &\approx \frac{1}{2\Delta t} \left(\left\langle \tilde{\varphi}_{\mathbf{k}}(t) | \tilde{\varphi}_{\mathbf{p}}(t+\Delta t) \right\rangle - \left\langle \tilde{\varphi}_{\mathbf{k}}(t+\Delta t) | \tilde{\varphi}_{\mathbf{p}}(t) \right\rangle \right) \end{split}$$

It is important to note that the NAC numerically calculated from eqn (7) may suffer from the phase inconsistencies issue, which can notably influence the charge dynamics. Phase consistency correction is required when simulating the nonadiabatic dynamics, as demonstrated by Akimov.⁷¹

2.5 PYXAID package

The TD-DFT/NA-MD calculations introduced above can be carried out using the PYXAID package, 50,72 as developed by

Akimov and Prezhdo. It is a Python/C++ based software for modeling quantum dynamics in systems composed of hundreds of atoms and involving thousands of electronic states. PYXAID implements multiple trajectory SH algorithms, including FSSH, 48 GFSH, 51 and DISH, 59 based on the CPA/NBRA. PYXAID includes several advanced functionalities, for instance, use of many-electron representation of the TD-KS equations, direct simulation of photoexcitation via explicit light-matter interaction, and Coulomb interactions between charges. PYXAID can adapt to several commercial and open-access computation packages including VASP,⁷³ Quantum Espresso,⁷⁴ DFTB+, 75 CP2K, 76 and QMflows. 77 The source code and handson tutorials are available on the website (https://quantumdynamics-hub.github.io/pyxaid/index.html). More recently, Li, Prezhdo and Akimov developed the PYXAID2 package (https:// github.com/Quantum-Dynamics-Hub/pyxaid2), utilizing the dynamic modules of the Libra code, 78 to include, for instance, spin-orbit coupling (SOC) in NA-MD simulations. In addition to PYXAID, other NA-MD codes capable of simulating excited state dynamics of condensed matter systems in the time-domain are available. For example, the Hefei-NAMD package of the Zhao group,³⁰ which shares many common functionalities with the PYXAID code. The TDAP package of the Meng group, 79 which is designed for modelling interaction between laser fields and solid-state materials in the basis of numerical atomic orbitals. The Kilin group⁸⁰ developed the NA-MD method based on the Redfield quantum master equation in the density matrix formalism. Other NA-MD codes include the NEXMD software of the Tretiak group,81 the NEWTON-X platform of the Barbatti group,82 the JADE code of the Lan group,83 and the SHARC package of the González group.⁸⁴ For a comprehensive account of NA-MD codes, readers are referred to the recent reviews by Crespo-Otero et al. and Smith et al. 45,46,85

Nonradiative electron-hole recombination under varying external conditions

MHPs share the chemical formula of ABX3, where "A" denotes the monovalent organic or inorganic cation (i.e., MA⁺, FA⁺, and Cs⁺), "B" denotes the divalent cation (i.e., Pb²⁺ and Sn²⁺), and "X" denotes the halide anion (i.e., Cl-, Br-, and I-, or their mixture), as illustrated in Fig. 1. By using different combination of elements, multidimensional perovskite structures pertaining to the same chemical formula can be formed. Two divalent cations "B" can be replaced with a pair of mono- and tri-valent cations. The ideal crystal structure of perovskites can be described as a network of corner-sharing [BX₆]⁴⁻ octahedra with "A" cations filling the cuboctahedral cavities. 86 Use of inorganic (i.e., Cs⁺) vs. organic (i.e., MA⁺) cations leads to different symmetries of the "A" species, spherical (Cs⁺) vs. non-spherical (MA⁺). This enables hybrid perovskites to exhibit additional orientational disorder and polarization compared to traditional inorganic semiconductors. Importantly, the crystal structure of MHPs is rather soft and anharmonic, as

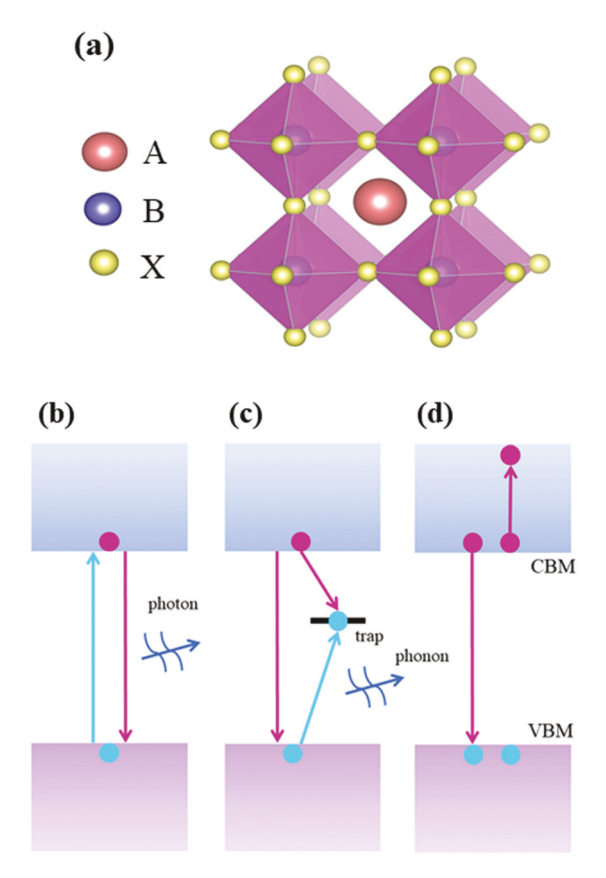


Fig. 1 (a) Typical crystal structures for ABX_3 perovskites (A = Cs⁺, MA⁺, FA⁺, etc.; B = Sn²⁺, Pb²⁺, etc.; X = Cl⁻, Br⁻, I⁻, etc.). Illustration of (b) radiative recombination, (c) non-radiative band-to-band recombination and trap-assisted recombination, (d) Auger recombination, which can contribute to both band-to-band and trap-assisted processes.

reflected by their low thermal conductivities, small bulk moduli, and large thermal expansion coefficients as well as considerable atomic displacements due to thermal fluctuations. Bistortions of the $[BX_6]^{4-}$ inorganic octahedra can thus happen easily under external perturbations such as pressure, temperature, electric field, etc. The degree of distortion of the $[BX_6]^{4-}$ octahedra can be characterized by the Goldschmidt tolerance factor, as introduced elsewhere.

Compressing a semiconductor crystal by hydrostatic pressure can decrease interatomic distances and engineer crystalline structures, presenting a means to tailor the electronic properties of materials. Pressure engineering has been successfully applied to many III–V semiconductors. Appling pressure in MHPs causes lattice deformation and alters the Pb–X bond length and Pb–X–Pb bond angle, as well as the interlayer spacing in layered perovskites. As a result, a variety of structural changes are introduced, including phase transitions, local distortions of the [PbX₆]^{4–} octahedra, and partial amorphization. ^{91–94} High pressure explorations also provide possibilities for new physical phenomena, such as the directindirect band gap transition, ⁹⁵ metallization, ⁹⁶ and dielectric tuning, ⁹⁷ enabling intriguing properties for applications in next generation photovoltaics. A number of groups reported

anti-correlation between band gap and carrier lifetime under pressure in 3D MAPbI₃ perovskite, ^{98,99} as well as stable 0D and 2D structures. ^{91,100,101} This is uncommon since, according to the energy gap law, ¹⁰² the lifetime decreases with decreasing band gap.

Using NA-MD simulation, Li et al. 103 rationalized the atomistic origin of the anticorrelation between carrier lifetime and band gap in the MAPbI₃ perovskite under compressive strain. Their results indicate that increasing pressures decrease Pb-I bond lengths and Pb-I-Pb angles, which brings the Pb and I atoms closer to each other and enhances the antibonding coupling between the Pb-s and I-p orbitals, contributing to the upshifting of the valence band maximum (VBM). As a result, the band gap of MAPbI₃ is smaller at higher pressure. In addition, higher pressure leads to larger fluctuation of Pb and I atoms, while suppressing the motion of MA cations. The destabilization of the inorganic lattice localizes electron and hole wavefunctions, decreasing their overlap, which is consistent with the mechanism previously proposed by Uratani et al. 104 Moreover, the decreased overlap between VBM and conduction band minimum (CBM) accelerates the coherence loss, and prolongs the charge carrier lifetime further, Fig. 2a. The decoherence in the time-domain is equivalent to the Franck-Condon overlap factor in the frequency domain, which reflects the vibrational density of states. 105,106 Smaller Franck-Condon factor, corresponding to faster decoherence, leads to slower excited-to-ground state transitions, according to the Fermi golden rule. As a result, nonradiative electron-hole recombination is reduced. The detailed atomistic understanding of the anticorrelation between carrier lifetime and energy gap of lead halide perovskites under compressive strain can be useful for further improvement of perovskite-based optoelectronic devices.

Ghosh et al. investigated the structures, electronic properties, and nonradiative recombination dynamics of FAPbI₃ under tensile strain by expanding the lattice. 107 It was shown that the applied tensile strain elongates the Pb-I bonds and increases the Pb-I-Pb bond angle, leading to a decreased [PbI₆]⁴⁻ octahedral tilting and a more symmetric phase of the entire lattice, as confirmed experimentally. The applied tensile strain changes the VBM and CBM levels, Fig. 2b and c. The data showed that the VBM levels shift down because of the decreased antibonding coupling of Pb-s and I-p orbitals due to elongated Pb-I bonds, while the CBM remains mostly unaffected because it is a nonbonding state. As a result, the band gap increases in an expanding lattice. NA-MD simulation further demonstrate that charge recombination slows down under tensile strain. The difference in the charge recombination rate can be explained in terms of the interplay between band gap, NAC, and decoherence time. When the lattice expands, spatial fluctuations of the inorganic [PbI₆]⁴⁻ increase since there is more space to distort the [PbI₆]⁴⁻ octahedron geometry, together with the reduced VBM-CBM overlap, leading to a larger NAC. The larger band gap indicates that more vibrational quanta are needed to absorb the energy dissipated from the electronic subsystem, and typically slows down

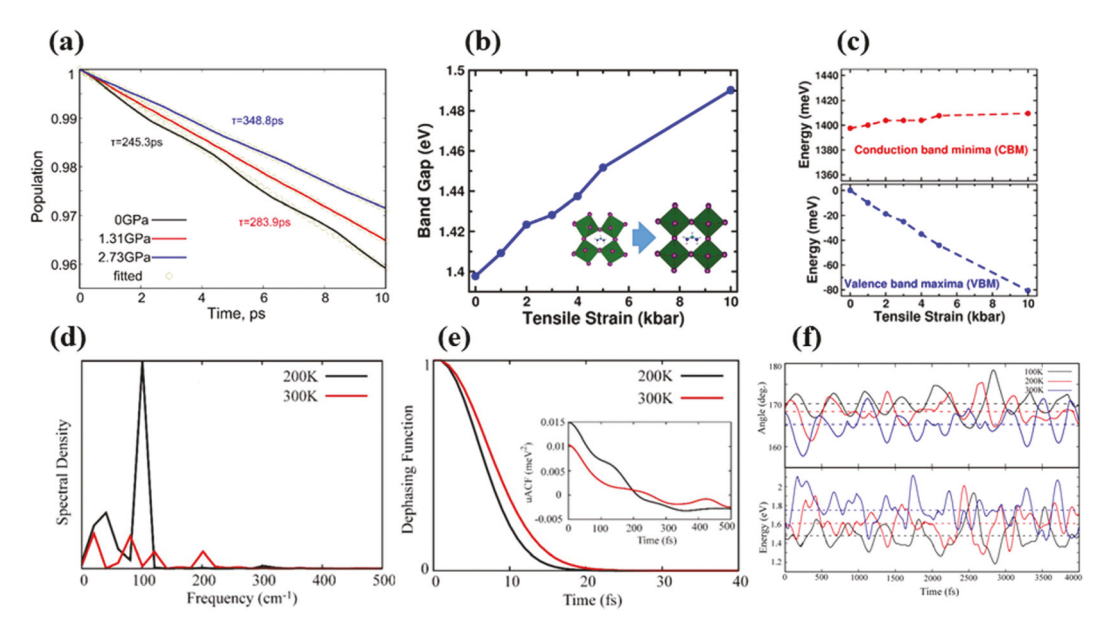


Fig. 2 (a) Excited-state population decay in MAPbl₃ at different pressures. Reproduced from ref. 103 with permission from American Chemical Society, copyright 2020. (b) Changes of the band gap and (c) the CBM and VBM levels under tensile strain. Reproduced from ref. 107 with permission from American Chemical Society, copyright 2019. (d) Spectral densities and (e) pure-dephasing functions for MAPbl₃ at different temperatures. Reproduced from ref. 109 with permission from American Chemical Society, copyright 2020. (f) Evolution of the Pb–Br–Pb bond angle and band gap in CsPbBr₃ at different temperatures. Reproduced from ref. 110 with permission from American Chemical Society, copyright 2018.

electron-hole recombination. The larger fluctuations of inorganic atoms under tensile strain activate a wider range of phonon modes available to couple to the electronic subsystem, leading to a faster decoherence process. Larger band gap and faster decoherence compete successfully with larger NAC in the FAPbI₃ perovskite with tensile strain, extending charge carrier lifetime, which is advantageous for solar cells operation. Long and coworkers performed a similar investigation and demonstrated that lattice expansion of mixed MA/FA perovskites suppresses nonradiative electron-hole recombination with the same mechanism.¹⁰⁸

The above works demonstrate that it is viable to fine-tune the lattice expansion or contraction to regulate the Pb-X bond length, the Pb-X-Pb bond angle, and distortion of [PbX₆]⁴⁻ octahedra to optimize the photovoltaic performance of perovskite materials. The internal strain arising from compositional engineering induces similar effects. For instance, one may consider changing both A-site organic (MA+, FA+, GA+) or inorganic (Cs⁺) cations, 111 B-site cations (Pb²⁺, Sn²⁺), 112 and halides (I-, Br-, Cl-)113,114 to achieve stable structures with desirable optoelectronic properties. Recent experiments reported that the lattice mismatch between perovskite films and substrates can induce significant strain within perovskites. 115 An alternative approach is to fine-tune the growth process during fabrication to incorporate residual compressive or tensile strain in the polycrystalline perovskite thin films, which is worthy of further investigation theoretically.

Solar cell devices are generally exposed to various weather conditions and subjected to heating during operation. It is thus important to investigate temperature-dependent photo-

physical properties of perovskite absorbers. Due to the novelty of PSCs devices, temperature-dependent studies in PSCs have so far been quite limited compared to the numerous studies on improving their efficiency. It is well-established that temperature strongly influences the dynamic properties of MAPbI₂, 116-120 For organic-inorganic hybrid perovskites, rotational motion of the organic cation couples to fluctuations of the inorganic lattice, leading to tilting of the [PbX₆]⁴⁻ octahedra. Temperature variations influence vibrations and rotations of the organic cations, mediate the organic-inorganic interactions, and correspondingly change the structural, electronic, and optical properties of hybrid perovskites. An unusual phenomenon is observed in MAPbI3: the energy gap increases, up to a few tens of meV, with increasing temperature, 87,121 although the change is not significant as compared to compositional engineering. This phenomenon contrasts with conventional semiconductors in which the energy gap decreases with rising temperature. 122,123 Moreover, several experimental reports proposed the negative thermal quenching mechanism in MAPbI3, namely, bimolecular bandto-band recombination slows down with rising temperature, and the decreased charge recombination extends carrier lifetime, resulting in an increase in $V_{\rm oc}$ and PCE. ^{19,124} This is also unexpected considering that the performance of semiconductor solar cells is known to decrease with increasing temperature. Understanding how temperature affects the structural dynamics of organic cations and inorganic sublattice and the charge-carrier dynamics of PSCs is therefore essential. these temperature-dependent photophysical However, phenomena have been described using simple models and

phenomenological interpretations of the time resolved photoluminescence measurements. Fundamental mechanisms underlying these temperature-related phenomena in PSCs required more detailed investigations.

Li et al. rationalized the unusual temperature dependence of nonradiative carrier relaxation in MAPbI₃ perovskite using NA-MD simulations. 109 They demonstrated that the atomistic mechanism of this peculiar behavior lies in the complex interplay of the inorganic and organic components of the hybrid perovskite. The distorted Pb-I lattice localizes electron and hole charge densities and enhances charge separation, a mechanism discussed above. The decreased charge density overlap weakens NAC, extending charge carrier lifetime. It was also found that rising temperature widens the band gap, in contrast to most semiconductors, in which temperature shrinks the band gap. Distortion of [PbX₆]⁴⁻ decreases the Pb-Br-Pb bond angle, weakens the anti-bonding coupling of Pb-s and I-p orbitals, and shifts down the VBM energy. CBM remains almost unchanged since it is a non-bonding state of Pb-p orbital. The two effects lead to increased band gap. Interestingly, rising temperatures decrease both inelastic and elastic electron-phonon scattering. The loss of quantum coherence slightly slows down at higher temperature, Fig. 2d and e, resulting in a reduced homogeneous optical linewidth, which is also unusual for most semiconductors. A combined experimental and theoretical work by Li, Madjet, and Miller 126 demonstrated that impulsively excited vibrational modes drive the structural distortion of MAPbI₃ after photoexcitation.

Recent experiments suggested that all-inorganic perovskites CsPbX₃ exhibit a similar temperature dependence of the charge carrier relaxation as the organic-inorganic hybrid perovskites. 127-129 Hybrid perovskites utilizing polar A-site organic cations exhibit additional orientational disorder, compared to all-inorganic perovskites, which contain non-polar spherical inorganic Cs⁺ cations, suggesting they may have different lattice dynamics. Interestingly, many experimental and theoretical investigations have reported highly anharmonic nuclear motion in MHPs, including all-inorganic CsPbBr₃, ^{130–132} which is unusual for efficient optoelectronic materials. The anharmonicity in MHPs originates from the double-well potential experienced by the halogen atoms vibrating perpendicularly to the bond connecting two Pb atoms, and can be captured by MD simulation based on DFT. 133,134 By employing a combination of TD-DFT and NA-MD, Li et al. demonstrated that anharmonic motions of Pb and Br atoms modulate NA electron-phonon coupling and non-radiative recombination dynamics in CsPbBr₃, 110 rationalizing the experimental observation. They found that, as temperature increases, the atoms in CsPbBr3 undergo substantial anharmonic motions. Stronger anharmonicity accelerates the coherence loss and increases carrier lifetimes despite an increased NA electron-phonon coupling at higher temperatures. The importance of anharmonic effects for optoelectronic properties of has been highlighted in a number of works. 130,133,135 In particular, it was reported that anharmonic motions result in narrowing of the Urbach tail in the absorption spectrum of CsPbBr₃.¹³⁰ Mayers *et al.*¹³¹ linked the large anharmonic displacement observed in hybrid perovskites with charge and orbital fluctuations and variation in the nonlinear electron–phonon coupling, in contrast to typical inorganic semiconductors. The data also show that rising temperature widens the CsPbBr₃ band gap, Fig. 2f, with the same mechanism applicable to MAPbI₃.

Zhou et al. 136 applied unsupervised machine learning to NA-MD and further rationalized this abnormal temperature dependence of carrier relaxation in MAPbI3. They found that fluctuations in MAPbI₃ structure are more important that the nuclear velocity in determining the NA coupling strength, and subsequently, the charge recombination dynamics. This is unexpected because NA electron-phonon coupling depends explicitly on the nuclear velocity. Moreover, they demonstrated that MA⁺ cations also influence charge recombination, even though they do not contribute to electron or hole wavefunctions. This is because rotational and center-of-mass motions of MA⁺ couple to fluctuation of the [PbI₆]⁴⁻ lattice. The I-I-I bond angle provide a better measure of NA coupling and band gap than octahedral Pb-I-Pb bond angle, as supported by machine learning analysis, Fig. 3. Hence, the I-I-I bond angle is the most dominant factor governing nonradiative electronphonon relaxation. The unsupervised machine learning analysis of NA-MD enables extraction of the most crucial factors influencing charge-phonon dynamics, which is of particular importance for PSCs performance.

In contrast to the anomalous temperature dependence of charge carrier relaxation in hybrid perovskites in the bulk phase, the nonradiative recombination at the interface between perovskite and other charge transporting materials follows the same trend with increasing temperature as in conventional semiconductors. Long and coworkers 137 investigated the nonradiative electron-hole recombination in the MAPbI₃/ NiO interface, and found that interfacial charge recombination is accelerated by a factor of 2 with temperature elevated from 100 K to 300 K. The variation of the carrier lifetimes with temperature is insignificant because temperature-induced thermal motions accelerate loss of quantum coherence, which competes with the larger NAC due to stronger electronvibrational interaction at higher temperature, Fig. 3f and g. Atomistic insights into the weak temperature dependence of charge recombination at interfaces between perovskites and charge extraction layers advance our fundamental understanding of the mechanisms of operation of PSCs.

In addition to the mechanical strain and temperature, the electronic and optical properties of hybrid perovskites are influenced by external electric fields. Han and Kilin¹³⁸ theoretically explored the influence of external electric fields on the optoelectronic properties of MHPs considering evolution of the reduced density matrix in the Redfield theory formalism. They adopted a model consisting of a CsPbBr₃ slab sandwiched between dye (hole transport layer) and TiO₂ (electron transport layer) with external electric fields normal to the surface of the perovskite slab. The applied external electric fields ranging within 50–100 meV Å⁻¹. According to their

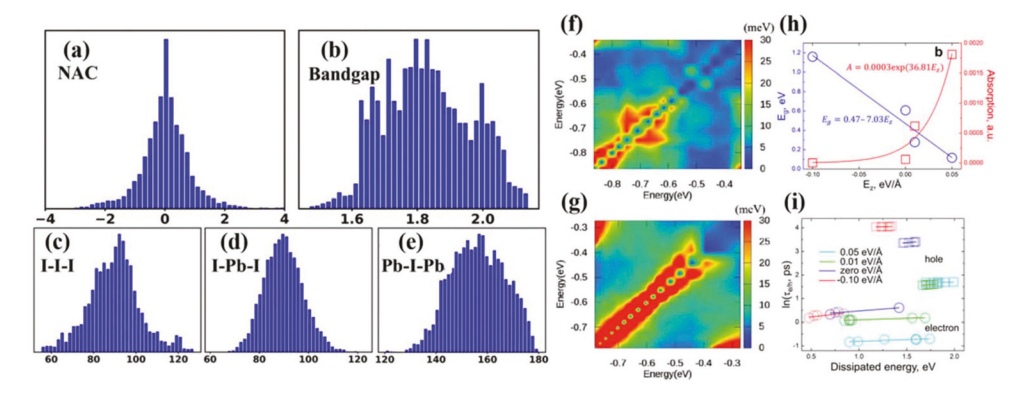


Fig. 3 Probability distributions of (a) NAC between HOMO and LUMO, (b) band gap, and (c) I–I–I, (d) I–Pb–I, (e) Pb–I–Pb bond angles. These angles have the highest mutual information with NAC and band gap among all geometric features and atomic motions. Reproduced from ref. 136 with permission from American Chemical Society, copyright 2020. Averaged NAC between states in the valence band for hole transfer across the MAPbI₃/NiO heterojunction at (f) 100 K and (g) 300 K. Reproduced from ref. 137 with permission from Royal Society of Chemistry, copyright 2019. (h) Influence of external electric field on energy gap and conductivity (absorbance at zero energy) of the thin film. (i) Relaxation time of electrons and holes as a function of excess energy for the thin film under various external electric field strengths. Reproduced from ref. 138 with permission from American Chemical Society, copyright 2020.

study, band gap increases linearly, and the conductivity diminishes exponentially with decreasing electric field strengths, Fig. 3h. NA-MD simulation of the interfacial electron and hole transfer showed that holes live longer than electrons at various electric fields, Fig. 3i. This is because the CB is denser near band gap than the VB, providing more chargephonon scattering channels. They also concluded that the charge carrier dynamics depend on the direction of external electric field, i.e., a positive electric field facilitates the relaxation of both electrons and holes whereas a negative electric field facilitates the relaxation of electrons but inhibits the relaxation of holes. This is because the sub-gap state shifts at different electric fields, activating the energy-gap law, 102 i.e., larger gap favors longer carrier relaxation. This work provides important insights into the relationship between external electric fields and the photophysical properties of PSC devices.

4 Unusual defects properties

Formation of intrinsic defects is inevitable in real situations during crystal growth and post-annealing treatment. The chemical and physical behavior of semiconductors, and their electronic properties in particular, are sensitive to presence of defects. A small concentration of free carriers in some conventional semiconductors is a direct consequence of defects. Defects are usually associated with dangling chemical bonds, which locally perturb lattice structure, modify atomic motions, and may (or may not) introduce states into the semiconductor band gap. Literature discussions of positions of defect energy levels center on shallow and deep gap states. ¹³⁹ Physically, a shallow state corresponds to a large orbital for a bound electron, typically 10–20 bulk interatomic distances in size. The energy gap between a shallow state and a band edge is in the range of a few $k_{\rm B}T$. In contrast, deep states correspond to small

orbitals a few interatomic distances in size. The energy gap between a deep state and a band edge is much larger than $k_{\rm B}T$. Shallow states are considered to be benign, offering a desirable means to optimize semiconductor electronic properties. In contrast, deep states introduce recombination centers that are capable of trapping free charge carriers, facilitating nonradiative, and sometimes radiative, electron-hole recombination.

Defects in solids can be classified into point defects, grain boundaries (GBs), extended surfaces, defect clusters, etc. Point defects in PSCs are particularly important because they play crucial roles in determining the materials' performance. The point defects can be further classified into missing lattice ions (vacancies), ions occupying irregular sites (interstitials), and impurity ions occupying regular lattice sites (substitutional defects). Anti-site disorder, in which a lattice ion replaces another lattice ion, can also be easily formed in hybrid perovskites. It has been observed that formation of charge traps in PSCs is correlated with these lattice point defects. Defects usually introduce deep gap states in conventional semiconductors, and thus, decrease device performance. 140,141 However, superior photovoltaic performance is obtained for PSCs, raising strong fundamental and applied interest. Many first-principle calculations on various perovskites have been carried out in the past decade. 6,142-149 It has been widely recognized that most deep level defects have high formation energy, whereas shallow level defects are easy to form. This behavior is known as "defect tolerance" and is frequently mentioned in the community. 6,150 Interpretation of the calculation is complicated by size of a simulation model, employed level of theory, and various experimental conditions. Experimental results have confirmed existence of multiple deep level defects in perovskite films through a series of characterization techniques. 151-154 In addition, although shallow traps do not form charge recombination centers, they may act as uninten-

tional doping sources and accelerate degradations in PSCs. ^{155,156} It is still not fully clear which defects are most likely to form, what happens to defect sites under PSC operating conditions, and which defects play the most crucial role in nonradiative energy losses.

Many first-principles calculations focused on point defects in PSCs, but mostly were limited to ground state properties, *i.e.*, defect structure and formation energy, charge transition level, electronic and optical properties, without proper treatment of elastic and inelastic electron–phonon interactions. In our recent perspective, ¹⁵⁷ we reviewed the roles of iodine interstitial, ^{158,159} iodine vacancy, ^{160,161} and Pb vacancy ¹⁶² in the charge carrier trapping and relaxation. We highlighted that charge recombination is sensitive to the oxidation state of these defects. ^{163,164,165}

Chu et al.88 have investigated the influence of various point defects on nonradiative electron-hole recombination in MAPbI₃. They focus on five point defects with low formation energy: iodine interstitial (I_i), MA substituted by iodine (MA_I) or Pb (MA_{Pb}), Pb vacancy (Pb_V), and iodine vacancy (I_V). They show that Ii and Pbv introduce shallow defect levels near the VBM, while MA_{Pb} and I_V introduce shallow defect levels near the CBM, Fig. 4a-f. MA_I is a deep level defect with energy 1.4 eV above the VBM. For all systems, thermal fluctuations of the defect levels along MD trajectories are larger compared to fluctuations of the VBM and CBM states, as rationalized by the fact that defect states are usually associated with broken bonds that are mobile during MD. The defect states are generally more localized in MHPs compared to conventional semiconductors due to the soft Pb-I inorganic lattice, and as a result, the localized defect states overlap less with VBM or CBM, leading to a small NAC and slow charge trapping and recombination. The simulated phonon spectra further demonstrate that only low-frequency modes participate in the nonradiative electron-phonon relaxation processes because of the soft Pb-I lattice composed of heavy elements.

For a typical photoexcitation process, recombination of electron and hole can occur either bypassing defect or via defect, Fig. 4g. By-defect recombination is known as trap-assisted electron-hole recombination and is generally complicated when multiple trap states are involved. Fig. 4h characterizes recombination via the two pathways. The results show that charge recombination in the defective systems is similar to that in the pristine system. Surprisingly, Ii shows the longest lifetime, suggesting that it could suppress the recombination process. This is in agreement with the previous time-domain ab initio investigation of I_i in MAPbI₃. ¹⁵⁹ The conclusions are applicable not only to hybrid perovskites, but also to the all-inorganic CsPbI₃ perovskite, which still has a soft inorganic lattice and low-frequency phonons even in the absence of organic cations, as reported in another work by Chu and Prezhdo.166 Such peculiar defect tolerance against nonradiative charge recombination has been rationalized by Zhang et al. 167 from the viewpoint of the strong lattice anharmonicity associated with deep level defects, based on the first-principle calculations. The conclusion drawn from these works is that both hybrid and all-in-

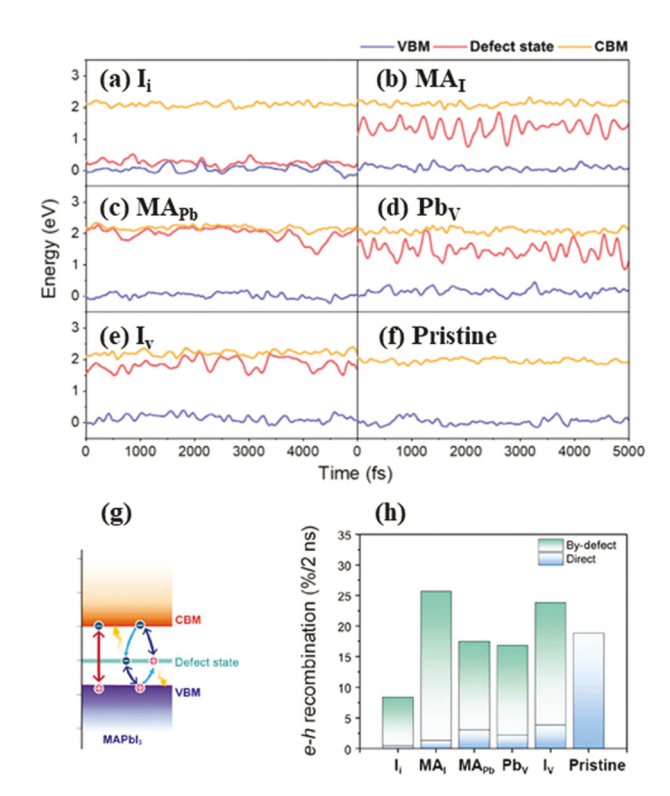


Fig. 4 (a to f) Evolution of VBM, CBM, and trap state energies for defective and pristine MAPbI₃ at 300 K. (g) Illustration of the direct and by-defect electron–hole recombination processes. (h) Charge recombination percentage for pristine and defective systems after 2 ns. Reproduced from ref. 88 with permission from American Association for The Advancement of Science, copyright 2020.

organic perovskites demonstrate unique defect tolerance. We expect this feature to be valuable in the design of novel semiconducting materials that have similar lattice properties.

Major losses undermining the performance of PSCs arise from inferior charge carrier transport at the contact layers. Two-dimensional transition metal dichalcogenides (TMDs), such as MoS_2 , are promising hole transport materials, owing to their excellent charge mobility. However, the MAPbI $_3/MoS_2$ interface shows a type I energy alignment due to the large work function (WF) of MoS_2 with respect to MAPbI $_3$, unfavorable for transfer of photo-excited holes from MAPbI $_3$ to MoS_2 . Experimental work by Peng *et al.* ¹⁶⁸ found that creation of sulfur vacancies (S_V) in MoS_2 with varying concentrations results in ultrafast hole transfer from perovskite to MoS_2 .

Using NA-MD, Shi *et al.*¹⁶¹ studied in detail how vacancy engineering affects the interface properties and the excited hole transport at TMD/perovskite interfaces. A relatively large WF of 4.35–5.49 eV was found in the pristine MoS₂/perovskite interface, inducing a negative band offset to form type I energy alignment, Fig. 5, hampering the hole transfer. Different surface terminations and MA arrangement in MAPbI₃ change the WF slightly. Introduction of S_V in MoS₂ leads to p-type doping, and correspondingly decreases the WF, but this is still insufficient to reverse the band offset. Interfacial iodine atoms

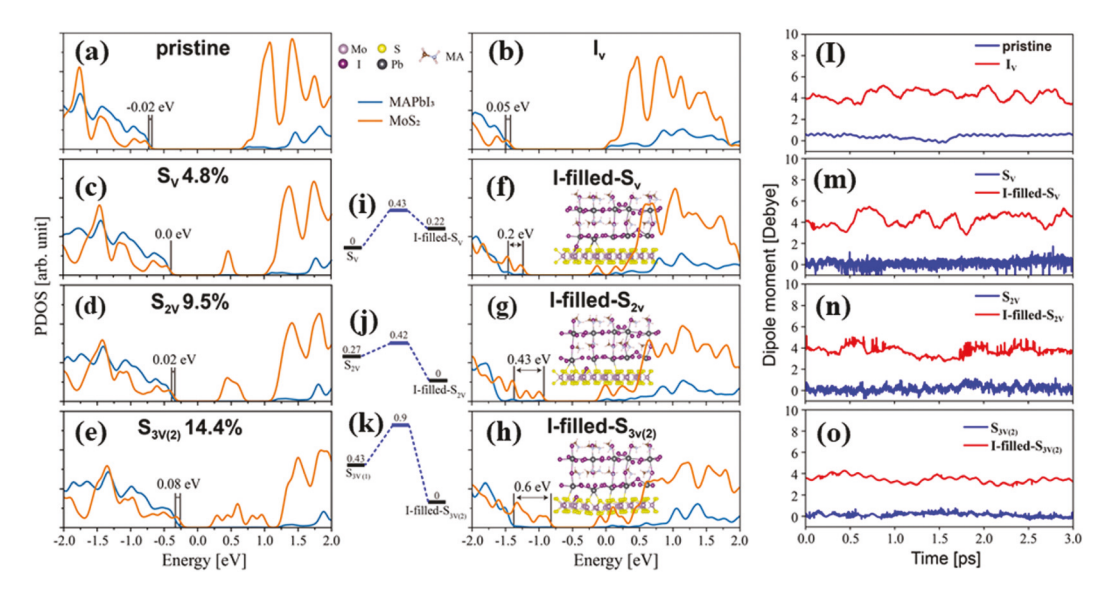


Fig. 5 PDOS of the MAPbl $_3$ /MoS $_2$ interface for (a) pristine, (b) I_v , (c-d) S_{nV} (n = 1-2), (e) $S_{3V(2)}$, and (f-h) corresponding I-filled configurations. (i-k) The calculated energy barriers of the S_v -to- I_v process. (l-o) Time evolved interface dipole moment at 300 K. Reproduced from ref. 161 with permission from American Chemical Society, copyright 2020.

can diffuse across the MAPbI $_3$ /MoS $_2$ interface to occupy the S $_V$ site in MoS $_2$ under thermal fluctuations, creating I $_V$ and an I-filled-S $_V$ defect at the MAPbI $_3$ interface. Nudged elastic band calculations show that relatively small iodine diffusion barriers facilitate this process, Fig. 5. Importantly, such a "S $_V$ -to-I $_V$ " chain generation of vacancies will induce an interfacial dipole moment and reverse the band offset between MoS $_2$ and MAPbI $_3$. NA-MD simulations show that the hole transfer from MAPbI $_3$ to MoS $_2$ will take place within several hundred femtoseconds, faster than the electron–hole recombination at vacancies by three orders of magnitude, further supporting excellent performance of MoS $_2$ as a hole transport layer.

Even though some point defects may be detrimental to carrier lifetimes in PSCs, they can be passivated using the impurity doping engineering strategy. For example, Iv in MAPbI₃ is a shallow donor, and can change into a deep acceptor when it is negatively charged (I_V⁻¹). In the I_V⁻¹ system, two Pb2+ ions near the vacancy site approach each other to form a Pb dimer¹⁶⁹ due to Coulomb attraction and create a deep level in the band gap, acting as a nonradiative electronhole recombination center. Our previous work showed that nonradiative charge recombination in MAPbI3 was extremely sensitive to the charge state of the iodine vacancy. 163 I_V^{-1} accelerated charge recombination by several orders of magnitude, whereas the positively charge iodine vacancy Iv +1 was electronically benign. In this case, Iv can be regarded as the DX center that involves transition between shallow and deep levels accompanied by large atomic displacements.

Motivated by this idea, Wang *et al.*¹⁷⁰ used NA-MD simulation to demonstrate that introduction of Br, which is more electronegative than iodine, can strengthen its chemical bond with Pb and prevent large atomic displacements associated with defect charging, Fig. 6. This efficiently mitigates defect

states and weakens NA electron–phonon coupling, extending the carrier lifetime from 3.2 ns in ${\rm I_V}^{-1}$ to 19 ns in the Br-doped ${\rm I_V}^{-1}$ system. Another work by Long and Prezhdo¹⁷¹ reported passivation of the iodine interstitial defect in MAPbI₃ by alkali ions. They demonstrated that the monovalent alkalis bind strongly to the interstitial iodine, and as a result, the energy of formation of the iodine interstitial defect increases significantly and defect concentration decreases. The defect level is removed since the introduced alkali eliminates the unsaturated valence of the interstitial iodine, extending the charge carrier lifetime, Fig. 6. These works generate an atomistic understanding of passivation effects by impurity doping in MAPbI₃ perovskites, providing a route to improve carrier lifetimes and device performance.

Recent work by Li et al. 172 demonstrated that alkali doping of the I_V defect in MAPbI₃ can also eliminate trap states and decrease charge recombination rate. They calculated the formation energy of MAPbI3 with and without the Iv defect after Li⁺-doping at the interstitial site (Li_i) or the B-site (Li_{pb}), *i.e.*, at a Pb atom near the vacancy site, and found that alkali cations prefer to occupy the B-site of the perovskite lattice. Iv introduces a sub-gap state capable of trapping holes and supported by Pb-p orbitals that interact across the vacancy site. Substitution of a Pb atom near Iv with an alkali metal breaks the Pb-p bonding state and removes extraneous electrons from the conduction band. NA-MD/TD-DFT simulation demonstrated that carrier lifetimes increase in the order $I_V \rightarrow Li \rightarrow$ Na \rightarrow K, agreeing with experimental observations. K⁺-Doped I_V system shows carrier lifetime exceeding 100 ns which is 3 times longer than the undoped system. Moreover, alkali doping perturbs system symmetry and localizes electron and hole charge densities, which weakens the NA coupling and accelerates the loss of quantum coherence in the electronic

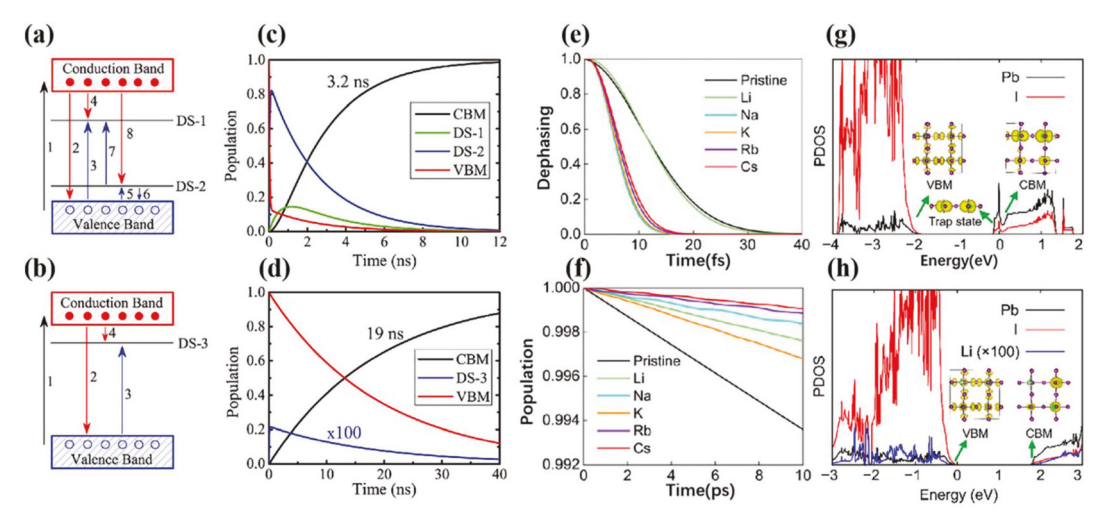


Fig. 6 Electron-hole recombination channels for the I_v^{-1} defect in (a) MAPbI₃ and (c) MAPb($I_{0.96}Br_{0.04}$)₃. (b and d) Evolution of populations of the key states defined in (a) and (c), respectively. Reproduced from ref. 170 with permission from Wiley-VCH, copyright 2019. (e) Pure-dephasing functions and (f) electron-hole recombination dynamics for the HOMO-LUMO transition in alkali-doped systems. Reproduced from ref. 171 with permission from Wiley-VCH, copyright 2020. Projected density of states (PDOS) for defective MAPbl₃ containing an iodine vacancy without (g) and with (h) Li doping. Reproduced from ref. 172 with permission from American Chemical Society, copyright 2021.

subsystem, slowing down the nonradiative charge recombination. This work provided detailed insights into the mechanism of defect passivation by alkali doping.

Long and coworkers¹⁷³ reported passivation of the Pb vacancy in MAPbI3 by water molecules. According to their findings, coexistence of a neutral Pb vacancy and water molecules shortens the carrier lifetime since it enhances the NAC and introduces a deep electron trap level. A negatively charged Pb vacancy interacts with water molecules, breaks the iodine dimer and eliminates the electron trap state, thereby, increasing the carrier lifetime and making it even longer than in the pristine system. In another work, Long and coworkers 174 investigated passivation of the iodine vacancy in MAPbI₃ by water molecules and a series of Lewis bases. They found that monodentate water, thiophene, and pyridine molecules can passivate one under-coordinated Pb ion, while bidentate 2-mercapto-pyridine (2-MP) and d-4-tert-butylphenylalanine (D4TBP) molecules can passivate two under-coordinated Pb ions. As a result, bidentate 2-MP and D4TBP bind more strongly than the monodentate passivators, this efficiently localizes VBM and CBM charge densities and decreases the NAC, leading to slower charge carrier recombination. These studies established the detailed mechanisms of defect passivation, and suggested specific guidelines for choosing passivating molecules to further improve PSC performance.

Another promising passivation strategy by oxygen treatment was recently reported. 175,176 It was demonstrated that oxygen molecules can have a positive effect on the charge carrier lifetime, despite undermining the stability of perovskite materials. 177-179 In addition to defect passivation, many works demonstrated that oxygen deteriorates stability of the MAPbI₃ crystal with light soaking. 180 This is because transfer of photoexcited electrons from perovskite to adsorbed oxygen molecules

assists the formation of superoxide and facilitates the degradation. 181 Long and coworkers 182 demonstrated that formation of superoxide in MAPbI₃ can be suppressed by introducing the electron accepting perylene diimide (PDI) molecule. A single oxygen molecule introduces a sub-gap state capable of trapping electron in MAPbI3, with electron trapping occurring within 1 ns. Introduction of a PDI molecule into the O₂-MAPbI₃ hybrid system creates another gap state above the O2-related trap state. NA-MD simulation revealed that CB electrons were trapped by the PDI-trap state rapidly, on the timescale of ~100 ps, reducing charge trapping by the O2-related state, which usually causes degradation and deteriorates optoelectronic properties.

Defect migration has been demonstrated to be the origin of anomalous properties in PSCs, including low photoconductivity response, current-voltage hysteresis, and switchable photovoltaic photocurrent. First-principle calculations predicted that the energy barrier for iodide migration is about 0.16 eV, 149 which gives the migration rate 7.7×10^{-10} s⁻¹ according to the Arrhenius equation $k=\frac{k_{\rm B}T}{\hbar}{\rm exp}{\left(-\frac{E_{\rm a}}{RT}\right)}$. The nanosecond ion

migration time falls into the range of nonradiative carrier lifetime in PSCs, as observed in many experimental and theoretical works. 4,5,157 The similarity in the timescales for the charge recombination and ion migration raises important questions of whether the two processes influence each other. Tong and Prezhdo¹⁸³ investigated the possible synergy between ion migration-induced Pb-I lattice distortion and charge carrier recombination in MAPbI3 using NA-MD simulations. After the start of migration of an iodide ion, the NAC value reaches its maximum value at approximately 2 ps, and reaches the second maximum value at approximately 3 ps. Both are very close to the two peaks in the distortion curve, as shown in Fig. 7, which shows that the strong distortion is

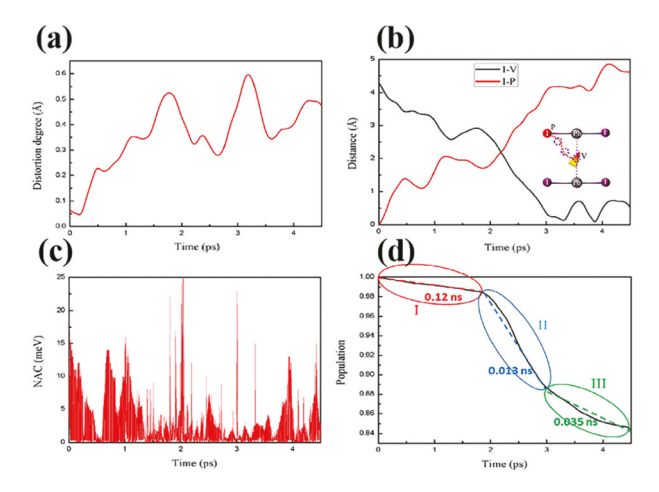


Fig. 7 (a) Averaged degree of distortion of the [Pbl₆]⁴⁻ octahedra adjacent to the migrating iodine. (b) Distances from the migrating iodine ion to the initial location (position P) and the final location (position V). (c) Time-dependent absolute NAC value during iodine migration. (d) Electron-hole recombination in the perovskite undergoing iodine migration. Reproduced from ref. 183 with permission from American Chemical Society, copyright 2020.

related to the increase in NAC. The migration of iodide ions is divided into pre-migration, migration, and post-migration. Premigration refers to the local equilibrium structure. Migration is the period when the iodide is moving between two local equilibrium structures. Post-migration is the period when the iodide has reached the new local equilibrium position but has not fully relaxed there yet. These three regimes give rise to different charge recombination dynamics. The nonradiative relaxation is fastest during migration of iodide ions, causing an order of magnitude reduction in the carrier lifetime. The simulation results demonstrate that different processes, such as ion migration and charge carrier recombination, are strongly correlated in PSCs, and that defects, considered benign for equilibrium geometries, can be very detrimental under non-equilibrium conditions.

Polycrystalline perovskite thin films contain interfaces between single-crystal grains known as GBs, which could significantly impact the optoelectronic performance of the devices. There has been ongoing debate in the PSCs community concerning the influence of GBs on charge carriers. Initial time-resolved photoluminescence spectroscopy studies suggested that GBs are detrimental to the charge carrier lifetimes and device performance in MAPbI₃. ^{184,185} Previous work by Long and Prezhdo¹⁸⁶ rationalized this observation and argued that doping GBs with Cl atoms can slow down nonradiative recombination. In contrast, Zhu and co-workers¹⁸⁷ pointed out that nonradiative recombination loss happens primarily along the non-GB regions of MAPbI3, suggesting favorable GBs properties. Using first-principle calculations, Yin et al. 188,189 showed that another GB structure in $MAPbI_3$ created no charge trap states, which was important for maintaining long carrier lifetimes. Yun et al. 190 further demonstrated that GBs in hybrid perovskites facilitate charge separation and transport through several experimental characterizations. However, only negative influences were reported for GBs of all-inorganic CsPbBr₃ perovskites. 191-193 The diverse and controversial experimental results raise important questions regarding the precise nature of perovskite GBs in determining the carrier lifetime and PSCs performance.

Using NA-MD/TD-DFT, Long and Prezhdo¹⁹⁴ investigated in detail the nonradiative recombination dynamics at the Σ 5 (310) GB of the MAPbI₃ perovskite. Such low index GBs can be conveniently imaged by transmission electron microscopy. They showed that the GB structure has a decreased band gap and shallow defect states with localized electron and hole wavefunctions, which help dissociate the photogenerated excitons. Reduction of the crystalline symmetry and the shallow trap states associated with the GB structure helped to separate electrons and holes, and to activate a broad range of phonon modes to couple with the charge carriers. Despite a stronger electronic-vibrational interaction and a smaller band gap, the decreased overlap of electron and hole wavefunctions reduced the NAC in the GB structure, maintaining the excited state lifetime as in the pristine system, Fig. 8. Involvement of more phonon modes in the GB system led to sub-10 fs coherence loss in the electronic subsystem, further helping to maintain long-lived charge carriers. Another work by Long and coworkers¹⁹⁵ investigated the impact of a different low index $\sum 5(210)$ GB structure on the charge dynamics in the all-inorganic CsPbBr3 perovskite. Interestingly, this GB structure had a larger NAC than the pristine CsPbBr3 system, whereas

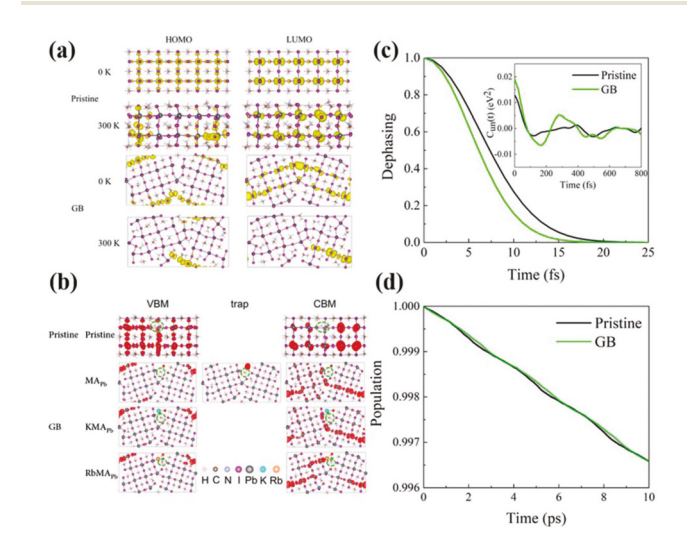


Fig. 8 (a) Distributions of HOMO and LUMO charge densities for pristine MAPbI $_3$ and $\Sigma 5(310)$ GB in their optimized ground state structures and at room temperature. (c) Pure-dephasing functions and (d) nonradiative charge recombination dynamics of pristine MAPbl₃ and Σ 5(310) GB. Reproduced from ref. 194 with permission from American Chemical Society, copyright 2019. (b) Charge densities of the key electronic states participating in charge trapping and recombination in MA_{Pb}@pristine MAPbI_3, MAPb@ Σ 5(310) GB of MAPbI_3, K-doped MAPb@ Σ 5(310) GB of $\text{MAPbI}_3\text{, and Rb-doped MA}_{\text{Pb}}\text{@}\Sigma5\text{(310)}$ GB of MAPbI $_3\text{.}$ Reproduced from ref. 195 with permission from American Chemical Society, copyright 2019.

the relative trend for the other quantities remained similar to MAPbI $_3$ with and without the $\sum 5(310)$ GB. 194 As a result, non-radiative recombination was accelerated moderately at the $\sum 5(210)$ GB of CsPbBr $_3$. The NAC was larger in the $\sum 5(210)$ GB of CsPbBr $_3$, in contrast to the $\sum 5(310)$ GB of MAPbI $_3$. 194 This could be ascribed to the involvement of a broad range of phonon modes in the NA relaxation due to symmetry breaking of the GB structure. These simulation results demonstrated that GBs can have both positive and negative influence on charge carrier dynamics in perovskites, as reported experimentally.

Previous experimental and theoretical works show that point defects easily accumulate at GBs. 196 Though MAPbI3 bulk is defect tolerant, GBs may be not. If deep level defects are presented at GBs, then they should be identified and passivated. Various attempts have been made to passivate GBs of MHPs. Long and Prezhdo¹⁹⁷ studied passivation of point defects at the $\sum 5(310)$ GB of MAPbI₃ by alkali ions using NA-MD simulations. They considered six configurations, including bulk MAPbI3 with and without the MAPb defect, the Σ5(310) GB of MAPbI₃ with and without the MA_{Pb} defect, and the $\Sigma 5(310)$ GB with the MA_{Pb} defect passivated by either K, or Rb. They found that the MA_{Pb} defect creates no sub-gap states and has little influence on the VBM and CBM of bulk MAPbI₃. As a result, the charge carrier lifetime is almost unchanged in the presence of the MAPb defect in bulk MAPbI3. In contrast, the MA_{Pb} defect forms an I-dimer in the GB system, and generates a deep sub-gap state, mediating recombination of photoexcited electrons and holes, and reducing the charge carrier lifetime. Furthermore, introduced K and Rb ions bind to the unsaturated halogen atoms, break the I-dimer, and remove the sub-gap state in the GB system. K- and Rb-doping weaken the NAC, decreases overlap of electron and hole charge densities, and shortens coherence in the electronic subsystem by introducing additional vibrational degrees of freedom. These factors lead to an increase of the charge carrier lifetimes by a factor of ~2 compared to the pristine MAPbI₃ perovskite. Future investigations should further connect different GBs structures in MHPs with optoelectronic properties, given the high number of controversial reports concerning the nature of GBs in PSCs, and assist in development of means to passivate GBs, if they act as nonradiative recombination center.

5 Photoexcitation dynamics in 2D perovskites

Quasi 2D layered perovskites exhibit superior environmental stability than their 3D counterparts, attracting much attention for applications in photovoltaics and optoelectronics. ^{198–200} The most common resultants are (100)-oriented 2D halide perovskites which can be classified in Ruddlesden–Popper (RP) phase, Dion–Jacobson (DJ) phase, alternating cations in the interlayer space (ACI), and those based on alkyl diammonium cations (DC). Among these configurations, the RP and DJ phases have been under most investigation at present. The

general formula of 2D perovskites is given as $(A')_2(A)_{n-1}B_nX_{3n+1}$ (RP phase) and $(A'')(A)_{n-1}B_nX_{3n+1}$ (DJ phase). Here, A' and A" are bulky monovalent and divalent organic cations, acting as insulating layers to separate layers of the inorganic framework. A, B, and X are the monovalent organic cation, divalent metal cation, and halide anion, respectively, present in the 3D perovskites discussed above. n denotes the number of layers. van der Waals interactions between the capping organic cations and the [BX₆]⁴⁻ framework, present in 2D perovskites, create additional energy required to break the perovskite structure. The outside chains of the capping organic cations are hydrophobic, leading to superior resistance to high-moisture and continuous lighting conditions. Unfortunately, photovoltaic efficiency of 2D perovskites is still relatively low because of the low absorption coefficients, large exciton binding energies, and poor out-of-plane charge transport caused by the insulating molecular cations. Many works have been devoted to optimizing 2D PSCs by lowering the band gap and reducing nonradiative electron-hole recombination through a variety of engineering strategies, such as introducing molecular cations with delocalized π -electrons, alternating the number of inorganic layers, doping with monovalent cations, and regulating crystallization kinetics. 199,201-203 Fundamental understanding of the photophysical processes governing the performance in 2D perovskites benefits from the quantum dynamics simulations.

The photophysical properties of 2D perovskites depend significantly on the long chain spacer cations, which not only define the thickness of the inorganic layers, but also influence their properties through steric distortion of the $[BX_6]^{4-}$ inorganic octahedra, electrostatic interactions and dynamic charge screening. At the same time, the spacer cations usually do not contribute to the band edge electronic properties directly. Using NA-MD simulations, Neukirch and coworkers²⁰⁴ investigated the non-radiative charge carrier recombination and dephasing processes in monolayer MHPs with RP and DJ phases differing in spacer cations. The investigated RP-phase A'2PbI4 perovskite contained two widely explored long-chain organic amine cations, CH₃(CH₂)₃NH₃⁺ (BA) and $C_6H_5(CH_2)_2NH_3^+$ (PEA). The DJ-phase APbI₄ perovskite contained the structurally well-characterized (aminomethyl)piperidinium (3AMP) cation. They demonstrated that phononinduced structural fluctuations strongly influence instantaneous charge localization and play critical roles in nonradiative charge recombination of 2D perovskites. They showed that the spacer divalent cation 3AMP in the DJ-phase perovskite introduced non-covalent interactions and induced interlayer coupling between perovskite slabs, which was absent in the RP-phase perovskite, efficiently stiffening the interlayer packing and reducing thermal fluctuations of the inorganic octahedra, Fig. 9. This leads to delocalization of band edge charge densities and smaller NAC, suppressing the charge recombination. The analysis revealed the atomistic origin of the lifetime difference in photoactive 2D perovskites with the DJ and RP phases.

Zhang *et al.*²⁰⁵ studied the hot electron cooling dynamics in 2D-layered perovskites compared to 3D perovskites, with emphasis on the role of spacer cations. Their results demon-

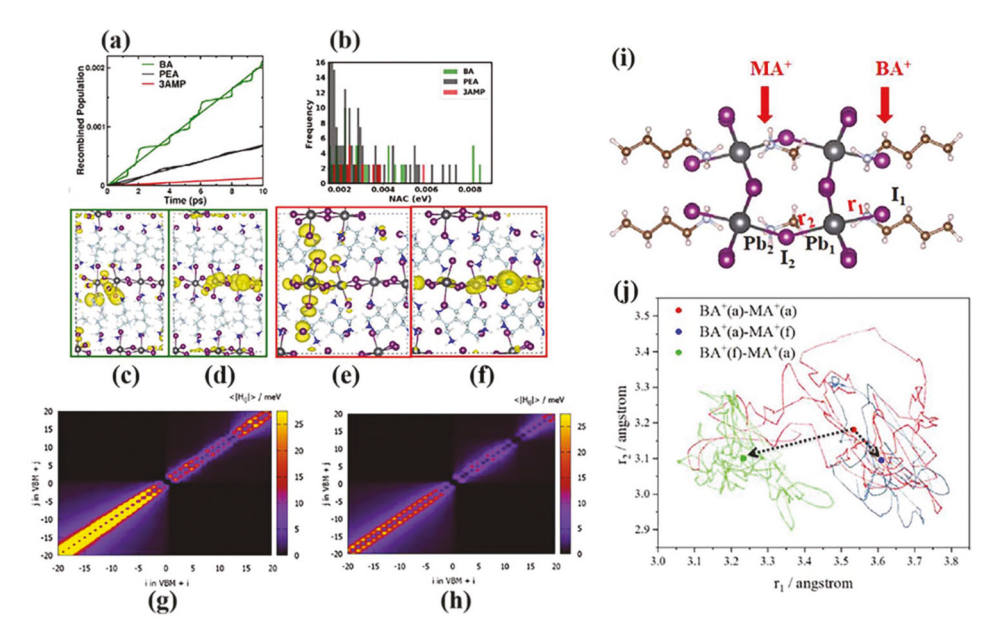


Fig. 9 (a) The excited state population in $(BA)_2PbI_4$, $(PEA)_2PbI_4$, $(PEA)_2PbI_4$, and $(3AMP)PbI_4$. (b) Probability distribution of absolute instantaneous NAC with magnitude larger than 1.5 meV. (c) VBM and (d) CBM charge densities for the $(BA)_2PbI_4$ configuration with the highest NAC. (e) VBM and (f) CBM charge densities for the $(3AMP)PbI_4$ configuration with the highest NAC. Reproduced from ref. 204 with permission from Royal Society of Chemistry, copyright 2020. Averaged absolute NAC in (g) [BA(a)-MA(f)] and (h) [BA(f)-MA(a)]. The negative and positive indices on the axes denote orbitals in the valence and conduction bands. (i) $(BA)_2(MA)Pb_2I_7$ structure illustrating the Pb_1-I_1 and Pb_1-I_2 bonds used to trace the structural fluctuations in the $[Pb_2I_7]^{3-}$ framework. (j) Trajectories showing the Pb_1-I_2 bond length (r_2) as a function of the Pb_1-I_1 bond length (r_1) . The solid circles in red, blue, and green refer to the mean values of r_2 and r_1 for the BA(a)-MA(a), BA(a)-MA(f), and BA(f)-MA(a) simulations, respectively. Reproduced from ref. 205 with permission from American Chemical Society, copyright 2019.

strated that hot electron relaxations in 2D (BA)₂(MA)Pb₂I₇ was faster than in 3D MAPbI₃, in agreement with experiment. They also studied the role of spacer cations in the carrier recombination. The large BA spacer cations in 2D (BA)₂(MA)Pb₂I₇ coupled more strongly to the Pb–I sub-lattice, leading to deformation of the inorganic framework and enhanced electron–phonon interactions, Fig. 9. Variation of NAC explained the lifetime differences in these systems.

Electrostatic charge screening influences the behavior of photogenerated charge carrier in 2D layer perovskites. 206,207 Yin et al. 208 carried out a joint experimental and theoretical investigations of the charge screening effect in 2D perovskites by combining ultrafast transient reflectance spectroscopy and time-domain NA-MD simulations, and demonstrated that the dielectric constant of the long chain spacer cations play an important role in regulating the electron cooling rate. They found that $(EA)_2PbI_4$ $(EA = HOC_2H_4NH_3^+)$ with a high dielectric constant organic spacer exhibits slower electron cooling compared to $(AP)_2PbI_4$ $(AP = HOC_3H_6NH_3^+)$ and $(PEA)_2PbI_4$ with low dielectric constants. The larger dielectric constant of the spacer cations better screened Coulomb interactions between electrons and holes, leading to a smaller NAC and a slower nonradiative intraband carrier relaxation, Fig. 10. The simulations results agreed well with the experimental characterizations. These simulations shed light on the importance of spacer cation engineering for further optimization of 2D layered perovskite optoelectronic devices.

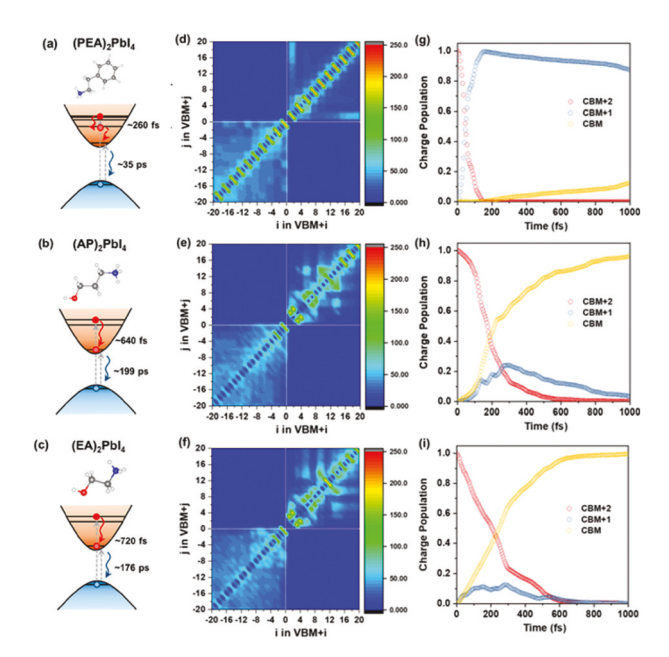


Fig. 10 (a–c) Hot electron relaxation and electron–hole recombination after a high-energy excitation, (d–f) averaged absolute NAC (in meV), and (g–i) hot electron relaxation dynamics in (PEA)₂PbI₄, (AP)₂PbI₄, and (EA)₂PbI₄. Reproduced from ref. 208 with permission from American Chemical Society, copyright 2019.

Jankowska and Prezhdo¹¹ investigated the influence of local electric order on the nonradiative electron-hole recombination in a ferroelectric lead halide perovskite using NA-MD simulations. The simulation focused on (BA)2PbCl4 with a roomtemperature stable ferroelectric phase, in which all polar C-N bonds were fully aligned. The considered structures also included the anti-ferro form with zero net electric dipole moment, and a mixed form of aligned and anti-aligned C-N bond pairs. The results demonstrated that electron-hole recombination was slower in the ferroelectric phase than the paraelectric phase. The band gaps and electronic properties were similar for all configurations; however, the NAC strengths were different due to charge separation induced by the cation ordering. In particular, the ferroelectric phase generally exhibited weaker NAC and larger band gap, Fig. 11, both factors favoring slower nonradiative carrier recombination. Fewer high-frequency phonon modes coupled to charges in the ferroelectric system, due to collective motions in the ordered phase, further rationalizing the reduced NAC. The simulations highlighted the important role of electric ordering in the charge carrier dynamics of MHPs. Even if the electric order is present only locally, and no thermodynamically stable electric phases are formed, still it can have a strong influence on the charge properties.

Long and Prezhdo²⁰⁹ investigated layer-dependence of non-radiative electron–hole recombination in RP-phase 2D perovs-kites using NA-MD. Focusing on $(BA)_2(MA)_{n-1}Pb_nI_{3n+1}$ with n=1 and 3, they showed that the trilayer $(BA)_2(MA)_2Pb_3I_{10}$ system had a smaller band gap owing to the weaker quantum confinement effect, compared to monolayer $(BA)_2PbI_4$. The small MA cations in the trilayer system rotated more freely than the larger BA cations between the layers, leading to distortion of the Pb–I inorganic lattice and larger NAC. The smaller band

gap and enhanced NAC should, in principle, accelerate charge recombination. However, the nonradiative relaxation in the trilayer system involved more high frequency modes due to the participation of lighter MA cations. This resulted in rapid loss of quantum coherence due to enhanced elastic electronphonon scattering. The coherence loss suppressed charge recombination, extending the excited state lifetimes, Fig. 11, in agreement with the experiments. Another work of Long and coworkers²¹⁰ also found a similar effect of quantum coherence by focusing on the 2D MA₃Bi₂I₉ perovskite interfaced with the 3D MAPbI₃ perovskite. These findings emphasized the positive influence of rapid loss of quantum coherence on charge carrier lifetimes in perovskite solar cells and related optoelectronic devices.

Experiments^{211,212} highlighted the importance of edge states in accelerating exciton dissociation and recombination of 2D perovskites. Long and Prezhdo²¹³ carried out NA-MD simulations of the RP-phase $(BA)_2(MA)_{n-1}Pb_nI_{3n+1}$ 2D perovskite with and without edges. Their results showed that charges get localized at perovskite edges. In particular, holes exhibit stronger localization than electrons because iodine and Pb atoms exhibit different chemistries. The undercoordinated non-metal iodine atoms at perovskite edges create localized states near the VBM capable of supporting holes. In comparison, metal Pb atoms are much more flexible to heal defects associated with unsaturated bonds, and therefore, chemically unsaturated Pb atoms confine electrons to a lesser extent. This is true for many nanoscale materials.214 It is worth noticing that localization of charges occurs not only at edges but also in bulk regions of 2D perovskites. The reason is that thermal atomic fluctuations induce distortion of the Pb-I lattice, leading to charge separation into different regions, as evidenced by the VBM and CBM charge density plots, Fig. 11.

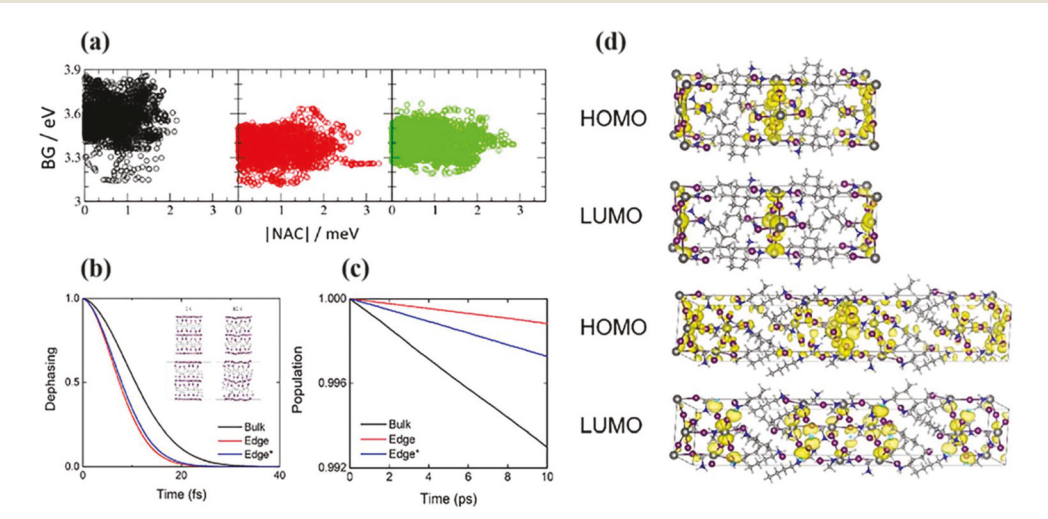


Fig. 11 (a) Correlation of band gap (BG) *versus* NAC for ferro, anti-ferro, and mixed (BA)₂PbCl₄. Reproduced from ref. 11 with permission from American Chemical Society, copyright 2017. (b and c) Pure-dephasing functions and electron—hole recombination dynamics for bulk, edge, and edge* in (BA)₂Pbl₄. Edge represents the HOMO–LUMO transition, while edge* is associated with the (HOMO–1)–(LUMO+1) transition, excluding HOMO and LUMO, which are the edge states. Reproduced from ref. 213 with permission from American Chemical Society, copyright 2019. (d) HOMO and LUMO charge densities for (BA)₂Pbl₄ and (BA)₂(MA)₂Pb₃l₁₀. Reproduced from ref. 209 with permission from American Chemical Society, copyright 2018.

This mechanism is different from polaron formation. The localization of charges at the edges is preserved under thermal fluctuations. The nonradiative recombination of electron and hole localized at edges takes a long time, because the well-separated charges lead to a small NAC and a rapid loss of quantum coherence between them. Another work of Long and coworkers²¹⁵ investigated the role of edge states on exciton dissociation and recombination in MAPbI3 bulk. Their study showed that edge states get localized due to breaking of lattice symmetry, decreasing the NAC and slowing down the charge recombination. These findings uncovered the important roles played by edges in MHPs and their dependence on edge chemistry and termination.

Hot carrier fluorescence and cooling

In photovoltaic cells, absorption of a photon with energy larger than the fundamental band gap produces "hot" carriers, which then relax to the VBM or CBM by exchanging energy with phonons. Harvesting hot carriers provides a promising route for increasing device efficiencies, since theoretically, efficiencies can be increased by 10% and more, compared to cold carrier utilization. One can use the extra energy stored in hot carriers to generate more carriers or extract hot carriers at contacts before their extra energy is converted to into heat, and the carriers are trapped or recombine. A reduced hot carrier cooling rate in solar absorbers is desirable for realizing efficient device operation. However, the carrier thermalization process in MHPs typically occur on a timescale of a few hundred femtoseconds, according to the ultrafast time-resolved spectroscopy characterization. 216,217 The sub-picosecond cooling times for hot carriers makes extracting them extremely challenging. Finding ways to slow down the carrier thermalization process can be important in further development of PSCs. Considerable experimental and theoretical efforts focus on this topic. Using first principle calculations, Kawai et al. 218 demonstrated that the sub-picosecond carrier cooling proceeds mainly through coupling to vibrations of the inorganic lattice. They also rationalized the slow hole cooling, reported experimentally from timeresolved spectroscopy measurements, to the narrow density of states in the spectral region of 0.6 eV above the VB top, which reduces the number of relaxation paths for the cooling.²¹⁸ By measuring the carrier cooling rate of MAPbI3 as a function of excitation energy density, Yang et al.219 demonstrated the existence of a phonon bottleneck effect, which causes a marked slowdown of carrier cooling at higher excitation densities. The same phenomena were also reported by other groups. 220,221 The slow cooling process can be explained in terms of the suppressed intraband transition rate close to band edges, and through other mechanisms, i.e., formation of polarons, 9 phonon up-conversion,²²² dielectric screening,²²³ quantum confinement, 221 low elastic stiffness of the lattice, 224 and Auger heating.²²⁵ Utilizing ultrafast "pump-push-probe" spectroscopy on MHP nanocrystal films, Bakulin and coworkers²²⁶ found

that the addition of cold carriers to the sample increases the carrier cooling rate, competing with the phonon bottleneck. Fundamental understanding of the charge carrier cooling and correlating these processes with perovskite structures will guide the design of efficient PSC devices.

Hot carrier cooling in MHPs can be tuned by compositional engineering. Madjet et al.227 carried out a time-domain ab initio investigation of carrier cooling dynamics in MAPbI₃ with and without Cl doping using NA-MD simulations. They identified the timescales of carrier cooling at different excess energies and phonon modes involved. They found that, for pristine MAPbI3, electron and hole cooling proceeds within ~700 fs, agreeing well with experiments. Hole relaxation was faster than electron relaxation, and Cl doping increased the difference, Fig. 12. This is because the VB supporting holes is denser than the CB supporting electrons. Denser electronic states lead to smaller energy level spacing, and NAC is inversely proportional to the level spacing. The reported correlation between the carrier cooling rate and density of states is consistent with the observation by Kawai et al. 218 Importantly, Cl doping extended both electron and hole cooling time. This is because the disorder created by the dopants induced moderate localization of wavefunctions in the conduction and valence bands, and the NACs between states inside both VB and CB were reduced. The authors showed further that the carrier intraband relaxation coupled strongly to the low-frequency modes associated with motions of I and Pb atoms. High-frequency modes related to the vibrational motion of MA also contributed to the carrier cooling, in contrast to the nonradiative relaxation across the band gap that nearly exclusively involves low-frequency phonons. The simulations showed that mixing halogen atoms in the perovskite materials is an efficient means to suppress the hot carrier cooling process to maximize extraction of hot carriers for realizing high-performing PSC devices.

Similar to the halogen anion doping, cation mixing is also a practical and successful means for regulating carrier cooling rates. Madjet et al.²²⁸ investigated intraband carrier relaxation in MHPs with three different cations, FAPbI3, MAPbI3, and CsPbI3, using NA-MD. The simulated carrier intraband relaxation times for each system agreed with experiments conducted at low excitation pump fluences. The carrier cooling process was mediated by the vibrational motions of I and Pb atoms. Interestingly, the hot carrier cooling dynamics were cation dependent. Longer carrier thermalization time was obtained for CsPbI₃ compared to the organic cations (MA and FA) based perovskites. The bulk modulus of FAPbI3 and MAPbI3 is smaller, and hence they are softer than CsPbI3. Larger size FA and MA are more likely to interact with the inorganic lattice, leading to deformation of the [PbI₆]⁴⁻ inorganic octahedra, while this effect was insignificant in CsPbI3. Interaction of the organic cations and the inorganic lattice alter the NAC and phonon modes participating in the nonradiative carrier relaxation. For MAPbI₃ and FAPbI₃, strong coupling of organic cation libration and torsion modes to low-frequency modes associated with Pb and I facilitated nonradiative carrier relaxation. This was further

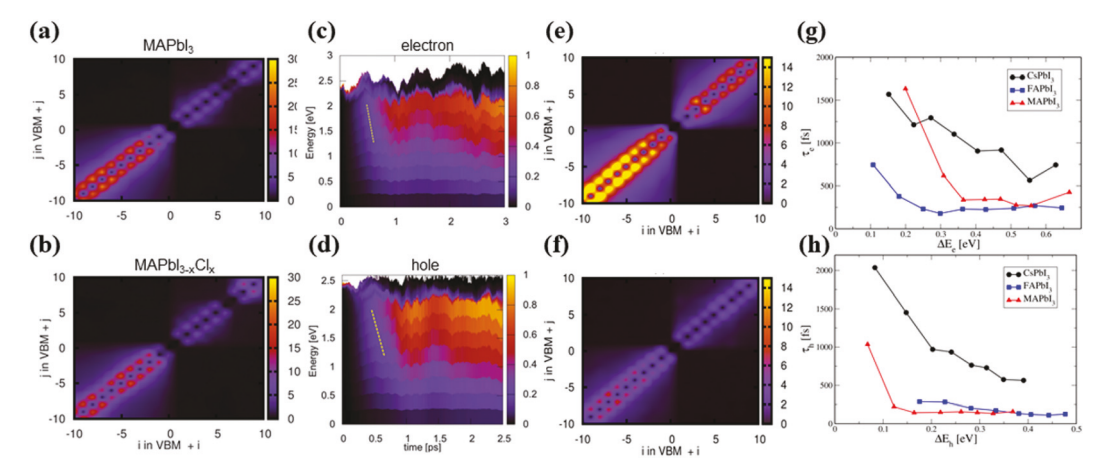


Fig. 12 Visualization of the averaged absolute NAC (in meV) between states in the space of KS orbital indices for (a) MAPbl₃ and (b) Cl-doped MAPbl₃. Reproduced from ref. 227 with permission from Royal Society of Chemistry, copyright 2016. 2D map representing (c) electron and (d) hole relaxation dynamics. Average absolute NAC (in meV) for MAPbl₃ when the MA molecules are free to move (e) and when they are frozen (f). Reproduced from ref. 228 with permission from American Chemical Society, copyright 2017. Cooling time of hot electrons (g) and hot holes (h) as a function of excess energies in CsPbl₃ (solid circles), FAPbl₃ (blue squares), and MAPbl₃ (red triangles). Reproduced from ref. 229 with permission from American Chemical Society, copyright 2018.

confirmed by considerable slowing of hot carrier cooling when the organic cations were artificially frozen, Fig. 11. Moreover, contribution of Cs to the VB and CB was negligible, while FA contribution was much more pronounced, as shown by the joint experimental and theoretical investigations. ¹⁶ The increased density of states in the presence of organic cations decrease the energy level spacing, and hence, increase the NAC. As a result, MAPbI₃ and FAPbI₃ showed faster carrier cooling than CsPbI₃, Fig. 12.

Intrinsic point defects can influence not only nonradiative electron-hole recombination but also hot carrier cooling. Lin-Wang Wang and coworkers²³⁰ studied the influence of the interstitial I2 defect on the carrier cooling process in MAPbI3 using NA-MD simulation with a density matrix formalism. Their results show that incorporation of interstitial I₂ produces linear I₄ moieties within the inorganic cage. The interstitial I₂ could also form additional bonds with nearby Pb atoms from [PbI₆]⁴⁻ octahedra. Such structural changes distort the Pb-I lattice, modulating the electronic properties and excited state dynamics of MHPs, Fig. 13. For example, the interstitial I2 system shows reduced DOS in the region near the CBM. In addition, the charge density of the CBM mainly localizes at the formed I₄-species in the defective system, whereas Pb-p orbitals dominate the CBM in pristine MAPbI₃. In contrast, the VB shows almost no changes after incorporation of the interstitial I2 defect. NA-MD simulations demonstrated that the interstitial I2 system exhibited a significantly prolonged electron cooling time and a modestly increased hole cooling time, as compared to pristine MAPbI₃. This can be rationalized by the following points. First, interstitial I₂ increases the contribution of I-p orbitals to the CBM, inducing changes of wave functions distribution. Second, the interstitial I₂ defect localizes the CB charge densities on the I4 moiety, decreases the overlap between CB states, and correspondingly weakens the NAC.

This work provided valuable insights into the long-lived hot electrons in PSCs achieved by the interstitial I₂ defect.

Experiments uncovered high-energy fluorescence in a hybrid organic-inorganic perovskite, corresponding to longlived hot charge carriers.²³¹ However, the same phenomenon was absent in an all-inorganic perovskite. Long and Prezhdo²³² rationalized the hot fluorescence in MAPbBr₃ using NA-MD. Their results suggested that reorientational motions of dipolar MA molecules influence the emission energy and carrier lifetime. Particularly, MAPbBr3 exhibits higher and lower band gap structures depending on MA orientations. The higher band gap structures have aligned MA cations characteristic of large "pancake" polarons, whereas the lower band gap structures arise from small polarons. Electron and hole wavefunctions of large polarons in the higher band gap structures are delocalized, leading to larger NAC and faster nonradiative charge recombination responsible for fluorescence decay. In comparison, electron and hole wavefunctions associated with small polarons produced lower band gap structures. Because small electron and hole polarons are strongly localized, Fig. 13a, the NAC between them is small, and the charge recombination is long. These results explained the shorter, several hundred picoseconds lifetime of hot fluorescence with respect to the nanosecond decay of the lower energy fluorescence. The simulation demonstrated that reorientation of the organic cations can lead to formation of different types of polarons, which explained long-lived hot fluorescence in organic-inorganic hybrid perovskites. In general, different types of structures in MHPs associated with defects, halide rich and poor phases, local electric order, etc. can act as different chromophores exhibiting emission at different energies and with different lifetimes.

Semiconductor quantum dots (QDs) represent a class of quasi-zero-dimensional materials whose size is smaller than

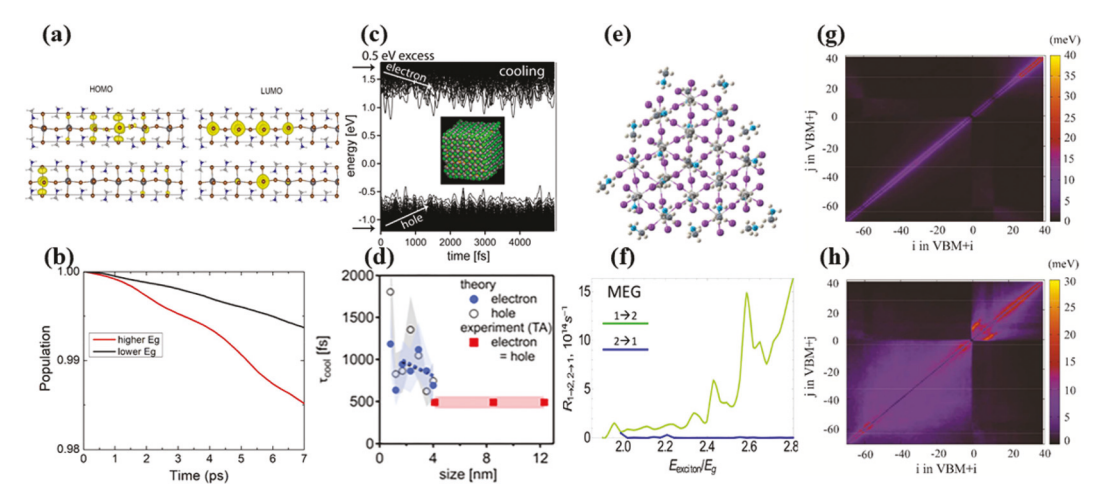


Fig. 13 (a) HOMO and LUMO charge densities in MAPbBr₃ of higher band gap (top) and lower band gap (bottom) structures. (b) Excited state population for MAPbBr₃ in the higher and lower band gap structures. Reproduced from ref. 232 with permission from American Chemical Society, copyright 2017. (c) Electron or hole is placed at 0.5 eV away from the respective band edge initially to simulate charge carrier cooling dynamics. (d) Simulated electron and hole cooling times, along with the experimental time constants. Reproduced from ref. 32 with permission from American Chemical Society, copyright 2020. (e) Atomistic model of a MAPbl₃ QD. (f) MEG and recombination rates as functions of the ratio of the initial excitation energy to the band gap. Reproduced from ref. 235 with permission from American Chemical Society, copyright 2017. (g and h) Ensemble averaged absolute NAC in MAPbI₃ with and without SOC. Reproduced from ref. 236 with permission from American Chemical Society, copyright 2018.

the corresponding Bohr excitonic radius, exhibiting properties different from 3D bulk semiconductors. Confinement of charges in QDs generate atom-like quantized spectral signals, and this effect strongly depends on QDs size. Generally, smaller size QDs have larger level spacing, which could suppress carrier thermalization due to the phonon bottleneck effect. Some experimental works suggested the existence of a hot phonon bottleneck in both hybrid organic-inorganic and all-inorganic perovskite QD. 219,233,234 By combining photoluminescence and absorption spectroscopies with time-domain NA-MD simulations, Infante and coworkers³² investigated the charge-carrier cooling process in CsPbBr3 QDs over a broad range of sizes from 0.8 to 12 nm, covering the strong to weak quantum confinement regime. Their findings demonstrated absence of the phonon bottleneck effect in CsPbBr₃ QDs. This is supported by the NA-MD data showing that the carrier cooling rate decreases only weakly with decreasing size of the CsPbBr₃ QDs, Fig. 13d, unlike the remarkedly long hot carrier lifetimes observed in other semiconductor QDs of small size, i.e., CdSe, due to the phonon bottleneck effect. Surprisingly, the cooling rate of electrons situated within 0.1 eV above the CBM was significantly decreased, by more than an order of magnitude. The authors rationalized this fact from the viewpoint of phonon-mediated fluctuations of the electronic structure. Electronic energy fluctuations assisted by phonons cause frequent state crossings near the CBM, see Fig. 13, producing persistent energetic electrons by the re-excitation process. Interestingly, the phonons available for driving energy fluctuations, and for coupling with charges, are strongly size dependent. Their theoretical studies agree well with experimental observations.

Multiple exciton generation (MEG) enables generation of multiple electron-hole pairs from a single photon excitation of

a semiconductor QD by utilizing photons with energies exceeding the band gap. MEG presents another strategy to maximize solar cell efficiency. Kilin and coworkers²³⁵ investigated the MEG dynamics in MAPbI₃ QDs using a NA-MD methodology in the many-body perturbation theory framework. They identified the timescales of various charge relaxation pathways including MEG, carrier cooling, and radiative and nonradiative electron-hole recombination in MAPbI₃ QDs. Their simulations showed that MEG is the fastest process, occurring on a femtosecond timescale, compared to the picosecond carrier cooling and nanosecond radiative/nonradiative carrier recombination. MEG was demonstrated to be the dominant pathway of carrier dynamics at early times. In addition, the MEG rate was found dependent on the excitation energy. The energy threshold required to generate any type of MEG process in the MAPbI₃ QD is twice the QD band gap, Fig. 13.

The above-mentioned studies ignored relativistic effects which are expected to be prominent in systems containing heavy elements. Consideration of such effects requires explicit incorporation of SOC into calculations. It has been reported in the literature that SOC notably influences the electronic properties of MHPs. However, influence of SOC on nonradiative carrier relaxation remains largely unexplored. Li, Prezhdo, and Akimov²³⁶ compared the electron and hole intraband relaxation in MAPbI3 with and without SOC. For this purpose, they developed a spinor formulation of NAC to account for the SOC effect in the NA-MD algorithm. They showed that SOC reduced the band gap by nearly ~1 eV. Moreover, SOC changes the wavefunction characteristics, enhancing the contribution of p_x and p_{ν} orbitals of Pb atoms to the CB and VB. NAC is significantly increased in the presence of SOC, Fig. 13g and h. As a result, electron and hole cooling rates are increased, producing

time scales in agreement with experiments. Relaxation of electrons and holes takes place by coupling to low-frequency vibrational modes associated with deformations of $[PbI_6]^{4-}$ octahedra. Using NA-MD simulation based on the two-components spinor, Cui and coworkers²³⁷ also reported the acceleration by SOC focusing on interfacial electron transfer in a C_{60} derivative (C_{60} -Py)/MAPbI₃ heterojunction. These findings demonstrated that SOC is important for correct and accurate assessment of the optoelectronic properties and charge carrier dynamics in materials containing heavy elements.

Akimov and coworkers²³⁸ investigated the nonradiative carrier cooling process in cubic and tetragonal phase CsPbI3 using a many-body NA-MD method. They found that the many-body description accelerated electron and hole intraband relaxation by a factor of 2.6 with respect to the single-particle description of the electronic excited states, bringing the timescale in better agreement with experiments. Stronger NAC between excited states under the many-body treatment is the dominant reason for the acceleration. They further demonstrated that the NAC is correlated with the degree of configurational mixing, as determined by the crystal symmetry. The cubic phase of CsPbI3, with a higher spatial symmetry, exhibits stronger mixing of excited Slater determinants than the tetragonal phase, and subsequently results in a faster nonradiative dynamics. Similar correlation between geometric symmetry and NAC strength was observed in the work of Tretiak and Fernandez-Alberti.²³⁹ Overall, incorporation of many-body effects in NA-MD simulation is important for accurate description of quantum dynamics.

7 Outlook

In this review, we have summarized the recent theoretical efforts aimed at modeling the photo-induced carrier dynamics in PSCs at the atomistic level, using advanced NA-MD methodologies in the framework of the TD-DFT formalism. Combination of TD-DFT and NA-MD allows one to study the competitive kinetics and nonequilibrium processes that determine the functionality and efficiency of solar cell devices on the time scales of electronic and atomic motions. By explicitly treating the elastic and inelastic electron-vibrational interactions and charge-charge scattering in the simulations, the mechanisms of charge carrier trapping and relaxation, charge and energy transfer, and interfacial charge separation and recombination in PSCs can be established. The timescales of these processes are identified and assigned with experiments. A thorough understanding of how various realistic factors govern each dynamical channel provides useful guidelines for improving the performance of devices relevant for solar energy conversion and optoelectronics. Below we highlight some directions for future studies.

7.1 Novel NA-MD algorithms should be developed to model excited state dynamics on long timescales

Currently, the computational expense of NA-MD simulations grows with system size and simulation time. In the quantum-

classical framework, the input into ab initio NA-MD simulations includes nuclear forces and NACs, as provided by onthe-fly electronic structure calculations. NACs require evaluation of time-derivatives of wavefunctions, or derivatives of wavefunctions or Hamiltonian with respect to nuclear coordinates. Typically, the electronic structure calculations constitute the most time-consuming part of the problem, and the CPA/ NBRA provides great computational savings. Propagation of EOM, eqn (5), can be time-consuming if processes involving many particles are involved, for example, Auger assisted charge trapping and recombination, and multiple exciton generation and recombination. In such case, the basis set used in eqn (5) can comprise hundreds of thousands of states, and sparse matrix techniques can be used to make the calculations more efficient. 240,241 More complex systems and processes increase the computational expense further. For example, large supercells should be adopted to model defects.²⁴² With periodic boundary conditions, the repeat unit should be sufficiently large to represent the host material and minimize periodic interactions between repeating defects. Simulations of large polarons require very large simulation cells as well, from few to tens of nanometers, which is beyond the reach of ab initio calculations. Fortunately, techniques for affordable NA-MD simulations in large-scale systems are under active development. To name a few, Lin-Wang Wang and coworkers²⁴³ developed a large-scale ab initio derived tightbinding model to directly simulate large polarons and their dynamics. Accelerated MD techniques, such as extended Lagrangian dynamics and force field simulations, can generate sufficiently long nuclear trajectories for NAC calculation and subsequent NA-MD. 244-247 Semiempirical approaches, i.e., the extended Hückel theory (EHT), 244,245,248,249 semi-empirical wavefunction methods,⁸¹ and DFTB+²⁵⁰⁻²⁵³ notably accelerate the electronic structure calculations, compared to ab initio DFT, and have been adopted for semiclassical NA-MD simulations of systems comprised of 1000 atoms or more, with promising results achieved. Larger systems can be studied with fragment-based techniques, such as the divide-andconquer (DC) or fragment molecular orbital (FMO) methods developed by the groups of Nakai, 254 Akimov, 251 Kitaura, 255 Blumberger, 256 and Prezhdo, 257 through interfacing with different quantum chemistry codes. Smith and Akimov²⁵⁸ applied the Landau–Zener (LZ) type formulas within the NBRA framework of NA-MD as an alternative to FSSH/NAMD. In the LZ-NAMD method, time-derivative wavefunctions and integration of TD-SE are not needed, and only electronic state energies are required, providing significant computational savings in NA-MD simulations of large systems. By sampling the vibronic Hamiltonian $[H_{ii} - i\hbar d_{ij}]$ from short time ab initio trajectories, obtaining fluctuation frequencies and amplitudes of Hamiltonian elements, and extending the Hamiltonian to arbitrary time, Akimov²⁵⁹ proposed the quasi-stochastic Hamiltonian (QSH) algorithm for longer dynamics. Alternatively, the vibronic Hamiltonian can be iterated multiple times to extend the simulations into nanoseconds, considering that nuclear contributions to the quantum dynamics

are dominated by thermal fluctuations that occur on picosecond timescales. 103,110 Machine learning (ML) is a promising strategy to accelerate NA-MD simulations by predicting the excited state properties for longer timescales based on costeffective training sets, without involving underlying quantum mechanics calculations. 130,249-266 The overall idea of OSH/ NA-MD is qualitatively similar to the ML/NA-MD simulation. So far, works on ML/NA-MD have focused primarily on molecular systems. Applications of ML/NA-MD to condensed matter systems, such as MHPs discussed herein, are of particular interest.267

7.2 Accuracy of NA-MD simulations depend on the electronic structure method

NA-MD simulation requires state energies and NACs as input. Low-cost bare DFT functionals, such as GGA/PBE, are unable to provide accurate band gap values for most semiconductors due to the self-interaction error. 268 Hybrid DFT functionals, i.e., HSE06,²⁶⁹ could partially correct the self-interaction error of GGA, and have been used to obtain accurate band gaps of semiconductors. More rigorous approaches for band gap predictions include quasi-particle GW calculations, 270 or the wavefunctionbased quantum Monte Carlo approaches, 271 both incurring significant computational expenses. The high-level ab initio multiple spawning (AIMS) method, which explicitly includes nuclear wavefunctions using a Gaussian basis, was adopted for NA-MD simulation of nonradiative recombination in a tiny perovskite QD, as performed by Levine and coworkers.²⁷² The influence of SOC on the electronic properties of systems with heavy elements, such as Pb or Br/I for MHPs, is strong. 33,273,274 SOC reduces the band gap of Pb based MHPs by nearly 1 eV. GGA calculations can provide band gaps that match experiments due to a fortuitous cancellation of the self-interaction error and neglect of SOC. It has been demonstrated that SOC can modify the bonding properties of perovskite materials without significant changes to the lattice structure, 33,275 as has been overlooked in most first-principle calculations. In addition to the structure modification and band gap reduction, SOC influences wavefunction properties, and should be included during NAC calculations for accurate NA-MD simulations. 236,272 The HSE06 functional, or the GW theory, can be used to correct the band gap if SOC is included. SOC, HSE06, and GW notably increase the computational cost, making them harder to apply with ab initio NA-MD. Different exchange-correlation functionals produce difference KS wavefunctions. PBE can significantly overestimate NAC compared to hybrid functionals, owing to erroneous delocalization of wavefunctions. 276,277 Overestimated by pure DFT functionals, NAC can be corrected by multiplication with a scaling factor obtained as the ratio of energy gaps computed using pure and hybrid functionals in a single point electronic structure calculation.²⁷⁶ The DFT+U and DFT+U+V approaches are often used to correct band gap energies and wavefunction delocalization predicted by GGA or LDA.²⁷⁸ A detailed comparison of nonradiative dynamics obtained with different exchange-correlation functionals and other levels of electronic structure theory is worthy of future investigations.

7.3 New theoretical frameworks and tools are required to model more complex physical processes and novel phenomena

Auger-type processes involving charge-charge scattering remain a relatively unexplored research area for NA-MD simulation. Examples include Auger-assisted charge separation, trapping and recombination, MEG and recombination, singlet fission, trion dynamics and higher order charge scattering processes. Auger processes are efficient in quantum confined nanoscale systems due to enhanced Coulomb interactions and larger densities of states. Experiments show that Auger recombination can be a dominant energy loss mechanism at high carrier concentrations in MHPs, causing efficiency drop. 279-282 Fundamental understanding of Auger processes from the atomistic viewpoint and development of strategies to reduce Auger recombination are important for further advances in PSCs. The progress relies on development of accurate and efficient computational methodologies. At present, Auger processes are primarily modelled time-independent phenomenological and pseudopotential methods, such as those developed and applied for calculation of Auger rates in III-V semiconductors by the van de Walle group. 283,284 However, various competing processes, including forward and inverse pure and phonon-assisted Auger processes, nonradiative charge-phonon trapping and relaxation, and radiative decay should be considered simultaneously, since they occur in parallel. 285 In addition, one might consider explicitly how realistic factors, such as dopants, defects and composition, influence Auger processes in PSCs. Time-domain ab initio simulation that closely mimics time-resolved experiments is the method of choice for such purposes. NA-MD implementations on top of the delta self-consistent field (Δ SCF) calculations, to explicitly include Coulomb, exchange, and correlation contributions, can provide a solution.²⁸⁶ Kilin and coworkers²³⁵ investigated the MEG dynamics in perovskite QDs by combining NA-MD and many-body perturbation theory. Auger-type quantum dynamics were investigated by Hyeon-Deuk et al.240,241 at the atomistic level using single-particle models, in which intermediate high-energy states were considered, and many-particle Auger transitions were decomposed into multiple single-particle transitions. The method was used to demonstrate an Auger-assisted electron transfer process. 287,288 Wang et al. 51,289 introduced the GFSH method to allow NA transitions involving multiple particles. The physics of Auger processes resides in carrier-carrier interactions, and therefore, such interactions should be included explicitly into NA-MD simulations, as done efficiently by Zhou et al. 290 Recently, excitonic effects were introduced into NA-MD simulation, with NAC calculated using both single particle and many-body bases, as achieved in the Libra platform interfaced with CP2K, developed by Akimov and coworkers, 31,238 and by the Zhao group in the Hefei-NAMD code.²⁹¹ Time-domain *ab initio* simulations of Auger processes involve huge numbers of states, significantly increasing computation demands.

Rapid development of quantum dynamics and ab initio approaches pave the way for further simulation advances in

this field. Methodological developments and realistic applications provide fundamental insights into the charge carrier dynamics of perovskites and other materials, further boosting the research and optimization of PSCs and optoelectronic devices

Conflicts of interest

There are no conflicts to declare.

Acknowledgements

W. L. acknowledges financial support of the National Natural Science Foundation of China (No. 21903023) and Natural Science Foundation of Hunan Province 2020JJ5225). O. V. P. acknowledges financial support of the U.S. National Science Foundation (CHE-1900510) and U.S. Department of Energy (DE-SC0014429).

References

- 1 N. J. Jeon, H. Na, E. H. Jung, T.-Y. Yang, Y. G. Lee, G. Kim, H.-W. Shin, S. Il Seok, J. Lee and J. Seo, Nat. Energy, 2018, 3, 682-689.
- 2 K. Yoshikawa, H. Kawasaki, W. Yoshida, T. Irie, K. Konishi, K. Nakano, T. Uto, D. Adachi, M. Kanematsu, H. Uzu and K. Yamamoto, Nat. Energy, 2017, 2, 1-8.
- 3 M. Nakamura, K. Yamaguchi, Y. Kimoto, Y. Yasaki, T. Kato and H. Sugimoto, IEEE J. Photovolt., 2019, 9, 1863-1867.
- 4 G. Xing, N. Mathews, S. Sun, S. S. Lim, Y. M. Lam, M. Gratzel, S. Mhaisalkar and T. C. Sum, Science, 2013, **342**, 344-347.
- 5 S. D. Stranks, G. E. Eperon, G. Grancini, C. Menelaou, M. J. P. Alcocer, T. Leijtens, L. M. Herz, A. Petrozza and H. J. Snaith, Science, 2013, 342, 341-344.
- 6 W.-J. Yin, T. Shi and Y. Yan, Appl. Phys. Lett., 2014, 104, 063903.
- 7 E. M. Hutter, M. C. Gélvez-Rueda, A. Osherov, V. Bulović, F. C. Grozema, S. D. Stranks and T. J. Savenije, *Nat. Mater.*, 2017, 16, 115-120.
- 8 F. Ambrosio, D. Meggiolaro, E. Mosconi and F. D. Angelis, J. Mater. Chem. A, 2020, 8, 6882-6892.
- 9 D. Meggiolaro, F. Ambrosio, E. Mosconi, A. Mahata and F. De Angelis, Adv. Energy Mater., 2020, 10, 1902748.
- 10 R. Shi, Z. Zhang, W. Fang and R. Long, Nanoscale Horiz., 2020, 5, 683-690.
- 11 J. Jankowska and O. V. Prezhdo, J. Phys. Chem. Lett., 2017, 8, 812-818.
- 12 Z.-G. Yu, Phys. Chem. Chem. Phys., 2017, 19, 14907-14912.
- 13 W. Shockley and H. J. Queisser, J. Appl. Phys., 1961, 32,
- 14 C. M. Sutter-Fella, Y. Li, M. Amani, J. W. Ager, F. M. Toma, E. Yablonovitch, I. D. Sharp and A. Javey, Nano Lett., 2016,

15 R. J. Stewart, C. Grieco, A. V. Larsen, J. J. Maier and J. B. Asbury, J. Phys. Chem. Lett., 2016, 7, 1148-1153.

- 16 J. Chen, M. E. Messing, K. Zheng and T. Pullerits, J. Am. Chem. Soc., 2019, 141, 3532-3540.
- 17 M. Ralaiarisoa, I. Salzmann, F.-S. Zu and N. Koch, Adv. Electron. Mater., 2018, 4, 1800307.
- 18 C. de Weerd, L. Gomez, A. Capretti, D. M. Lebrun, E. Matsubara, J. Lin, M. Ashida, F. C. M. Spoor, L. D. A. Siebbeles, A. J. Houtepen, K. Suenaga, Y. Fujiwara and T. Gregorkiewicz, Nat. Commun., 2018, 9, 4199.
- 19 R. L. Milot, G. E. Eperon, H. J. Snaith, M. B. Johnston and L. M. Herz, Adv. Funct. Mater., 2015, 25, 6218-6227.
- 20 S. Guo, Y. Zhao, K. Bu, Y. Fu, H. Luo, M. Chen, M. P. Hautzinger, Y. Wang, S. Jin, W. Yang and X. Lü, Angew. Chem., 2020, 132, 17686-17692.
- 21 Q. Li, Z. Chen, B. Yang, L. Tan, B. Xu, J. Han, Y. Zhao, J. Tang and Z. Quan, J. Am. Chem. Soc., 2020, 142, 1786–1791.
- 22 L. Wang, R. Long and O. V. Prezhdo, Annu. Rev. Phys. Chem., 2015, 66, 549-579.
- 23 R. Long, O. V. Prezhdo and W. Fang, Wiley Interdiscip. Rev.: Comput. Mol. Sci., 2017, 7, e1305.
- 24 O. V. Prezhdo, Acc. Chem. Res., 2009, 42, 2005-2016.
- 25 O. V. Prezhdo, W. R. Duncan and V. V. Prezhdo, Acc. Chem. Res., 2008, 41, 339-348.
- 26 X. Zhao and R. Long, J. Phys. Chem. Lett., 2020, 11, 10298-10305
- 27 C. F. Craig, W. R. Duncan and O. V. Prezhdo, Phys. Rev. Lett., 2005, 95, 163001.
- 28 W. Jia, Z. Cao, L. Wang, J. Fu, X. Chi, W. Gao and L.-W. Wang, Comput. Phys. Commun., 2013, 184, 9–18.
- 29 D. J. Vogel and D. S. Kilin, J. Phys. Chem. C, 2015, 119, 27954-27964.
- 30 Q. Zheng, W. Chu, C. Zhao, L. Zhang, H. Guo, Y. Wang, X. Jiang and J. Zhao, Wiley Interdiscip. Rev.: Comput. Mol. Sci., 2019, 9, e1411.
- 31 B. Smith, M. Shakiba and A. V. Akimov, J. Chem. Theory Comput., 2021, 17, 678-693.
- 32 S. C. Boehme, S. ten Brinck, J. Maes, N. Yazdani, F. Zapata, K. Chen, V. Wood, J. M. Hodgkiss, Z. Hens, P. Geiregat and I. Infante, Nano Lett., 2020, 20, 1819-1829.
- 33 S. Yun, X. Zhou, J. Even and A. Hagfeldt, Angew. Chem., Int. Ed., 2017, 56, 15806-15817.
- 34 F. Gao, Y. Zhao, X. Zhang and J. You, Adv. Energy Mater., 2019, 10, 1902650.
- 35 S. Akin, N. Arora, S. M. Zakeeruddin, M. Grätzel, R. H. Friend and M. I. Dar, Adv. Energy Mater., 2020, 10, 1903090.
- 36 D. Yang and D. Huo, J. Mater. Chem. C, 2020, 8, 6640-6653.
- 37 R. M. Williams and R. Brakkee, DOI: 10.20944/preprints202003.0375.v1.
- 38 D. Luo, R. Su, W. Zhang, Q. Gong and R. Zhu, Nat. Rev. Mater., 2020, 5, 44-60.
- 39 L. Lin and N. M. Ravindra, SN Appl. Sci., 2020, 2, 1361.
- 40 D. Ghosh, E. Welch, A. J. Neukirch, A. Zakhidov and S. Tretiak, J. Phys. Chem. Lett., 2020, 11, 3271–3286.

395502.

- 41 K. Drukker, J. Comput. Phys., 1999, 153, 225-272.
- 42 O. V. Prezhdo, J. Chem. Phys., 1999, 111, 8366-8377.
- 43 C. Brooksby and O. V. Prezhdo, *Chem. Phys. Lett.*, 2001, 346, 463–469.
- 44 T. R. Nelson, A. J. White, J. A. Bjorgaard, A. E. Sifain, Y. Zhang, B. Nebgen, S. Fernandez-Alberti, D. Mozyrsky, A. E. Roitberg and S. Tretiak, *Chem. Rev.*, 2020, 120, 2215– 2287.
- 45 R. Crespo-Otero and M. Barbatti, *Chem. Rev.*, 2018, **118**, 7026–7068.
- 46 B. Smith and A. V. Akimov, *J. Phys.: Condens. Matter*, 2019, 32, 073001.
- 47 A. V. Akimov and O. V. Prezhdo, in *Encyclopedia of Nanotechnology*, ed. B. Bhushan, Springer Netherlands, 2015, pp. 1–20.
- 48 J. C. Tully, J. Chem. Phys., 1990, 93, 1061-1071.
- 49 Y.-S. Wang, P. Nijjar, X. Zhou, D. I. Bondar and O. V. Prezhdo, *J. Phys. Chem. B*, 2020, **124**, 4326–4337.
- 50 A. V. Akimov and O. V. Prezhdo, *J. Chem. Theory Comput.*, 2013, **9**, 4959–4972.
- 51 L. Wang, D. Trivedi and O. V. Prezhdo, J. Chem. Theory Comput., 2014, 10, 3598–3605.
- 52 G. Miao and J. Subotnik, *J. Phys. Chem. A*, 2019, **123**, 5428-5435.
- 53 J. E. Subotnik, A. Jain, B. Landry, A. Petit, W. Ouyang and N. Bellonzi, Annu. Rev. Phys. Chem., 2016, 67, 387– 417.
- 54 S. V. Kilina, A. J. Neukirch, B. F. Habenicht, D. S. Kilin and O. V. Prezhdo, *Phys. Rev. Lett.*, 2013, **110**, 180404.
- 55 O. Postupna, R. Long and O. V. Prezhdo, *J. Phys. Chem. C*, 2015, **119**, 12088–12094.
- 56 O. Postupna, H. M. Jaeger and O. V. Prezhdo, *J. Phys. Chem. Lett.*, 2014, 5, 3872–3877.
- 57 B. F. Habenicht, O. N. Kalugin and O. V. Prezhdo, *Nano Lett.*, 2008, **8**, 2510–2516.
- 58 S. Kilina, K. A. Velizhanin, S. Ivanov, O. V. Prezhdo and S. Tretiak, *ACS Nano*, 2012, **6**, 6515–6524.
- 59 H. M. Jaeger, S. Fischer and O. V. Prezhdo, *J. Chem. Phys.*, 2012, **137**, 22A545.
- 60 J.-K. Ha, I. S. Lee and S. K. Min, J. Phys. Chem. Lett., 2018, 9, 1097–1104.
- 61 S. K. Min, F. Agostini, I. Tavernelli and E. K. U. Gross, J. Phys. Chem. Lett., 2017, 8, 3048–3055.
- 62 A. Jain and J. E. Subotnik, J. Phys. Chem. Lett., 2015, 6, 4809–4814.
- 63 H.-T. Chen and D. R. Reichman, J. Chem. Phys., 2016, 144, 094104.
- 64 J. E. Subotnik, J. Phys. Chem. A, 2011, 115, 12083-12096.
- 65 N. Shenvi, J. E. Subotnik and W. Yang, *J. Chem. Phys.*, 2011, **134**, 144102.
- 66 O. V. Prezhdo and P. J. Rossky, J. Chem. Phys., 1997, 107, 5863–5878.
- 67 O. V. Prezhdo and P. J. Rossky, J. Chem. Phys., 1997, 107, 825–834.
- 68 A. V. Akimov and O. V. Prezhdo, *J. Phys. Chem. Lett.*, 2013, 4, 3857–3864.

- 69 B. Smith and A. V. Akimov, J. Chem. Phys., 2019, 151, 124107.
- 70 S. Hammes-Schiffer and J. C. Tully, J. Chem. Phys., 1994, 101, 4657–4667.
- 71 A. V. Akimov, J. Phys. Chem. Lett., 2018, 9, 6096-6102.
- 72 A. V. Akimov and O. V. Prezhdo, J. Chem. Theory Comput., 2014, 10, 789–804.
- 73 G. Kresse and J. Hafner, *Phys. Rev. B: Condens. Matter Mater. Phys.*, 1993, 47, 558–561.
- 74 P. Giannozzi, S. Baroni, N. Bonini, M. Calandra, R. Car, C. Cavazzoni, D. Ceresoli, G. L. Chiarotti, M. Cococcioni, I. Dabo, A. D. Corso, S. de Gironcoli, S. Fabris, G. Fratesi, R. Gebauer, U. Gerstmann, C. Gougoussis, A. Kokalj, M. Lazzeri, L. Martin-Samos, N. Marzari, F. Mauri, R. Mazzarello, S. Paolini, A. Pasquarello, L. Paulatto, C. Sbraccia, S. Scandolo, G. Sclauzero, A. P. Seitsonen, A. Smogunov, P. Umari and R. M. Wentzcovitch, J. Phys.: Condens. Matter, 2009, 21,
- 75 B. Hourahine, B. Aradi, V. Blum, F. Bonafé, A. Buccheri, C. Camacho, C. Cevallos, M. Y. Deshaye, T. Dumitrică, A. Dominguez, S. Ehlert, M. Elstner, T. van der Heide, J. Hermann, S. Irle, J. J. Kranz, C. Köhler, T. Kowalczyk, T. Kubař, I. S. Lee, V. Lutsker, R. J. Maurer, S. K. Min, I. Mitchell, C. Negre, T. A. Niehaus, A. M. N. Niklasson, A. J. Page, A. Pecchia, G. Penazzi, M. P. Persson, J. Řezáč, C. G. Sánchez, M. Sternberg, M. Stöhr, F. Stuckenberg, A. Tkatchenko, V. W.-z. Yu and T. Frauenheim, J. Chem. Phys., 2020, 152, 124101.
- 76 T. D. Kühne, M. Iannuzzi, M. Del Ben, V. V. Rybkin, P. Seewald, F. Stein, T. Laino, R. Z. Khaliullin, O. Schütt, F. Schiffmann, D. Golze, J. Wilhelm, S. Chulkov, M. H. Bani-Hashemian, V. Weber, U. Borštnik, M. Taillefumier, A. S. Jakobovits, A. Lazzaro, H. Pabst, T. Müller, R. Schade, M. Guidon, S. Andermatt, N. Holmberg, G. K. Schenter, A. Hehn, A. Bussy, F. Belleflamme, G. Tabacchi, A. Glöß, M. Lass, I. Bethune, C. J. Mundy, C. Plessl, M. Watkins, J. VandeVondele, M. Krack and J. Hutter, J. Chem. Phys., 2020, 152, 194103.
- 77 F. Zapata, L. Ridder and J. Hidding, *QMflows*, Zenodo, 2017.
- 78 A. V. Akimov, J. Comput. Chem., 2016, 37, 1626-1649.
- 79 C. Lian, M. Guan, S. Hu, J. Zhang and S. Meng, *Adv. Theory Simul.*, 2018, **1**, 1800055.
- 80 A. Forde, T. M. Inerbaev, E. K. Hobbie and D. S. Kilin, *J. Am. Chem. Soc.*, 2019, **141**, 4388–4397.
- 81 W. Malone, B. Nebgen, A. White, Y. Zhang, H. Song, J. A. Bjorgaard, A. E. Sifain, B. Rodriguez-Hernandez, V. M. Freixas, S. Fernandez-Alberti, A. E. Roitberg, T. R. Nelson and S. Tretiak, J. Chem. Theory Comput., 2020, 16, 5771–5783.
- 82 M. Barbatti, M. Ruckenbauer, F. Plasser, J. Pittner, G. Granucci, M. Persico and H. Lischka, *Wiley Interdiscip. Rev.: Comput. Mol. Sci.*, 2014, 4, 26–33.
- 83 L. Du and Z. Lan, *J. Chem. Theory Comput.*, 2015, **11**, 1360–1374.

84 S. Mai, P. Marquetand and L. González, Wiley Interdiscip. Rev.: Comput. Mol. Sci., 2018, 8, e1370.

Nanoscale

- 85 M. Barbatti and R. Crespo-Otero, in *Density-Functional Methods for Excited States*, ed. N. Ferré, M. Filatov and M. Huix-Rotllant, Springer International Publishing, Cham, 2016, pp. 415–444.
- 86 Q. A. Akkerman and L. Manna, ACS Energy Lett., 2020, 5, 604–610.
- 87 W. A. Saidi, S. Poncé and B. Monserrat, *J. Phys. Chem. Lett.*, 2016, 7, 5247–5252.
- 88 W. Chu, Q. Zheng, O. V. Prezhdo, J. Zhao and W. A. Saidi, *Sci. Adv.*, 2020, **6**, eaaw7453.
- 89 T. A. Tyson, W. Gao, Y.-S. Chen, S. Ghose and Y. Yan, *Sci. Rep.*, 2017, 7, 9401.
- 90 V. M. Goldschmidt, Naturwissenschaften, 1926, 14, 477-485.
- 91 Y. Yuan, X.-F. Liu, X. Ma, X. Wang, X. Li, J. Xiao, X. Li, H.-L. Zhang and L. Wang, Adv. Sci., 2019, 6, 1900240.
- 92 Y. Wang, S. Guo, H. Luo, C. Zhou, H. Lin, X. Ma, Q. Hu, M. Du, B. Ma, W. Yang and X. Lü, *J. Am. Chem. Soc.*, 2020, 142, 16001–16006.
- 93 X. Zhou and Z. Zhang, AIP Adv., 2020, 10, 085210.
- 94 M. I. Saidaminov, J. Kim, A. Jain, R. Quintero-Bermudez, H. Tan, G. Long, F. Tan, A. Johnston, Y. Zhao, O. Voznyy and E. H. Sargent, *Nat. Energy*, 2018, 3, 648–654.
- 95 C. Gao, R. Li, Y. Li, R. Wang, M. Wang, Z. Gan, L. Bai, Y. Liu, K. Zhao, S. F. Liu, Y. Cheng and W. Huang, *J. Phys. Chem. Lett.*, 2019, 10, 5687–5693.
- 96 A. Jaffe, Y. Lin, W. L. Mao and H. I. Karunadasa, *J. Am. Chem. Soc.*, 2017, **139**, 4330–4333.
- 97 A. Jaffe, Y. Lin and H. I. Karunadasa, *ACS Energy Lett.*, 2017, 2, 1549–1555.
- 98 L. Kong, G. Liu, J. Gong, Q. Hu, R. D. Schaller, P. Dera, D. Zhang, Z. Liu, W. Yang, K. Zhu, Y. Tang, C. Wang, S.-H. Wei, T. Xu and H. Mao, *Proc. Natl. Acad. Sci. U. S. A.*, 2016, 113, 8910–8915.
- 99 G. Liu, L. Kong, J. Gong, W. Yang, H. Mao, Q. Hu, Z. Liu, R. D. Schaller, D. Zhang and T. Xu, *Adv. Funct. Mater.*, 2017, 27, 1604208.
- 100 T. Yin, B. Liu, J. Yan, Y. Fang, M. Chen, W. K. Chong, S. Jiang, J.-L. Kuo, J. Fang, P. Liang, S. Wei, K. P. Loh, T. C. Sum, T. J. White and Z. X. Shen, *J. Am. Chem. Soc.*, 2019, **141**, 1235–1241.
- 101 J. C. Beimborn, L. R. Walther, K. D. Wilson and J. M. Weber, *J. Phys. Chem. Lett.*, 2020, **11**, 1975–1980.
- 102 M. Bixon, J. Jortner, J. Cortes, H. Heitele and M. E. Michel-Beyerle, *J. Phys. Chem.*, 1994, **98**, 7289–7299.
- 103 W. Li, Z. Chen, J. Tang and O. V. Prezhdo, *Chem. Mater.*, 2020, 32, 4707–4715.
- 104 H. Uratani and K. Yamashita, J. Phys. Chem. C, 2017, 121, 26648–26654.
- 105 O. V. Prezhdo and P. J. Rossky, *Phys. Rev. Lett.*, 1998, **81**, 5294–5297.
- 106 O. V. Prezhdo and P. J. Rossky, *J. Chem. Phys.*, 1997, **107**, 5863–5878

- 107 D. Ghosh, D. Acharya, L. Zhou, W. Nie, O. V. Prezhdo, S. Tretiak and A. J. Neukirch, *J. Phys. Chem. Lett.*, 2019, **10**, 5000–5007.
- 108 Y. Wang and R. Long, J. Phys. Chem. Lett., 2020, 11, 1601–1608.
- 109 W. Li, J. Tang, D. Casanova and O. V. Prezhdo, ACS Energy Lett., 2018, 3, 2713–2720.
- 110 W. Li, A. S. Vasenko, J. Tang and O. V. Prezhdo, *J. Phys. Chem. Lett.*, 2019, **10**, 6219–6226.
- 111 J. He, W.-H. Fang, R. Long and O. V. Prezhdo, ACS Energy Lett., 2018, 3, 2070–2076.
- 112 R. Shi and R. Long, J. Phys. Chem. Lett., 2019, 6604-6612.
- 113 J. Liu and O. V. Prezhdo, *J. Phys. Chem. Lett.*, 2015, 6, 4463–4469.
- 114 J. He, A. S. Vasenko, R. Long and O. V. Prezhdo, *J. Phys. Chem. Lett.*, 2018, **9**, 1872–1879.
- 115 Y. Chen, Y. Lei, Y. Li, Y. Yu, J. Cai, M.-H. Chiu, R. Rao, Y. Gu, C. Wang, W. Choi, H. Hu, C. Wang, Y. Li, J. Song, J. Zhang, B. Qi, M. Lin, Z. Zhang, A. E. Islam, B. Maruyama, S. Dayeh, L.-J. Li, K. Yang, Y.-H. Lo and S. Xu, Nature, 2020, 577, 209–215.
- 116 B. Murali, E. Yengel, W. Peng, Z. Chen, M. S. Alias, E. Alarousu, B. S. Ooi, V. Burlakov, A. Goriely, M. Eddaoudi, O. M. Bakr and O. F. Mohammed, *J. Phys. Chem. Lett.*, 2017, 8, 137–143.
- 117 S. Shrestha, G. J. Matt, A. Osvet, D. Niesner, R. Hock and C. J. Brabec, *J. Phys. Chem. C*, 2018, **122**, 5935–5939.
- 118 S. Sun, Z. Deng, Y. Wu, F. Wei, F. H. Isikgor, F. Brivio, M. W. Gaultois, J. Ouyang, P. D. Bristowe, A. K. Cheetham and G. Kieslich, *Chem. Commun.*, 2017, 53, 7537–7540.
- 119 M. C. Gélvez-Rueda, D. H. Cao, S. Patwardhan, N. Renaud, C. C. Stoumpos, G. C. Schatz, J. T. Hupp, O. K. Farha, T. J. Savenije, M. G. Kanatzidis and F. C. Grozema, *J. Phys. Chem. C*, 2016, 120, 16577–16585.
- 120 M. A. Carignano, S. A. Aravindh, I. S. Roqan, J. Even and C. Katan, *J. Phys. Chem. C*, 2017, 121, 20729–20738.
- 121 B. J. Foley, D. L. Marlowe, K. Sun, W. A. Saidi, L. Scudiero, M. C. Gupta and J. J. Choi, *Appl. Phys. Lett.*, 2015, **106**, 243904.
- 122 K. P. O'Donnell and X. Chen, *Appl. Phys. Lett.*, 1991, 58, 2924–2926.
- 123 Y. P. Varshni, Physica, 1967, 34, 149-154.
- 124 S. Kahmann, O. Nazarenko, S. Shao, O. Hordiichuk, M. Kepenekian, J. Even, M. V. Kovalenko, G. R. Blake and M. A. Loi, ACS Energy Lett., 2020, 5, 2512–2519.
- 125 D. H. Fabini, G. Laurita, J. S. Bechtel, C. C. Stoumpos, H. A. Evans, A. G. Kontos, Y. S. Raptis, P. Falaras, A. Van der Ven, M. G. Kanatzidis and R. Seshadri, *J. Am. Chem.* Soc., 2016, 138, 11820–11832.
- 126 H.-G. Duan, V. Tiwari, A. Jha, G. R. Berdiyorov, A. Akimov, O. Vendrell, P. K. Nayak, H. J. Snaith, M. Thorwart, Z. Li, M. E. Madjet and R. J. D. Miller, *J. Am. Chem. Soc.*, 2020, 142, 16569–16578.
- 127 C. Yu, Z. Chen, J. J. Wang, W. Pfenninger, N. Vockic, J. T. Kenney and K. Shum, *J. Appl. Phys.*, 2011, **110**, 063526.

Review

- 128 Q. Han, W. Wu, W. Liu, Q. Yang and Y. Yang, *J. Lumin.*, 2018, **198**, 350–356.
- 129 C. Wolf and T.-W. Lee, *Mater. Today Energy*, 2018, 7, 199–207.
- 130 C. Gehrmann and D. A. Egger, *Nat. Commun.*, 2019, **10**, 3141.
- 131 M. Z. Mayers, L. Z. Tan, D. A. Egger, A. M. Rappe and D. R. Reichman, *Nano Lett.*, 2018, **18**, 8041–8046.
- 132 T. Lanigan-Atkins, X. He, M. J. Krogstad, D. M. Pajerowski, D. L. Abernathy, Guangyong N. M. N. Xu, Z. Xu, D.-Y. Chung, M. G. Kanatzidis, S. Rosenkranz, R. Osborn and O. Delaire, *Nat. Mater.*, 2021, 1–7.
- 133 J. Yang, Y. Wang, T. Wu and S. Li, *Chem. Mater.*, 2020, 32, 2470-2481.
- 134 M. A. Carignano, S. A. Aravindh, I. S. Roqan, J. Even and C. Katan, J. Phys. Chem. C, 2017, 121, 20729–20738.
- 135 Y.-N. Wu, W. A. Saidi, J. K. Wuenschell, T. Tadano, P. Ohodnicki, B. Chorpening and Y. Duan, *J. Phys. Chem. Lett.*, 2020, 11, 2518–2523.
- 136 G. Zhou, W. Chu and O. V. Prezhdo, *ACS Energy Lett.*, 2020, 5, 1930-1938.
- 137 J. He, W. Fang and R. Long, *J. Mater. Chem. A*, 2019, **8**, 607–615.
- 138 Y. Han and D. S. Kilin, *J. Phys. Chem. Lett.*, 2020, 9983–9989.
- 139 M. Lannoo, *Point Defects in Semiconductors I: Theoretical Aspects*, Springer-Verlag, Berlin Heidelberg, 1981.
- 140 K. Morigaki, *Physics of Amorphous Semiconductors*, World Scientific, 1999.
- 141 H. J. Queisser and E. E. Haller, Science, 1998, 281, 945–950.
- 142 A. Buin, P. Pietsch, J. Xu, O. Voznyy, A. H. Ip, R. Comin and E. H. Sargent, *Nano Lett.*, 2014, 14, 6281–6286.
- 143 M. L. Agiorgousis, Y.-Y. Sun, H. Zeng and S. Zhang, *J. Am. Chem. Soc.*, 2014, **136**, 14570–14575.
- 144 M. H. Du, J. Mater. Chem. A, 2014, 2, 9091-9098.
- 145 J. Kim, S.-H. Lee, J. H. Lee and K.-H. Hong, *J. Phys. Chem. Lett.*, 2014, 5, 1312–1317.
- 146 H. Shi and M.-H. Du, *Phys. Rev. B: Condens. Matter Mater. Phys.*, 2014, **90**, 174103.
- 147 A. Buin, R. Comin, J. Xu, A. H. Ip and E. H. Sargent, *Chem. Mater.*, 2015, 27, 4405–4412.
- 148 M.-H. Du, J. Phys. Chem. Lett., 2015, 6, 1461-1466.
- 149 J. M. Azpiroz, E. Mosconi, J. Bisquert and F. D. Angelis, *Energy Environ. Sci.*, 2015, **8**, 2118–2127.
- 150 R. E. Brandt, V. Stevanović, D. S. Ginley and T. Buonassisi, *MRS Commun.*, 2015, 5, 265–275.
- 151 Y. Chen and H. Zhou, J. Appl. Phys., 2020, 128, 060903.
- 152 X. Wen, Y. Feng, S. Huang, F. Huang, Y.-B. Cheng, M. Green and A. Ho-Baillie, *J. Mater. Chem. C*, 2016, 4, 793–800.
- 153 H.-S. Duan, H. Zhou, Q. Chen, P. Sun, S. Luo, T.-B. Song,B. Bob and Y. Yang, *Phys. Chem. Chem. Phys.*, 2014, 17, 112–116.
- 154 N. Liu, P. Liu, H. Zhou, Y. Bai and Q. Chen, *J. Phys. Chem. Lett.*, 2020, **11**, 3521–3528.

- 155 V. V. Brus, F. Lang, J. Bundesmann, S. Seidel, A. Denker, B. Rech, G. Landi, H. C. Neitzert, J. Rappich and N. H. Nickel, Adv. Electron. Mater., 2017, 3, 1600438.
- 156 S. Tan, I. Yavuz, M. H. Weber, T. Huang, C.-H. Chen, R. Wang, H.-C. Wang, J. H. Ko, S. Nuryyeva, J. Xue, Y. Zhao, K.-H. Wei, J.-W. Lee and Y. Yang, *Joule*, 2020, 4, 2426–2442.
- 157 W. Li, R. Long, J. Tang and O. V. Prezhdo, J. Phys. Chem. Lett., 2019, 10, 5798–5807.
- 158 X. Zhang, M. E. Turiansky, J.-X. Shen and C. G. Van de Walle, *Phys. Rev. B*, 2020, **101**, 140101.
- 159 W. Li, J. Liu, F.-Q. Bai, H.-X. Zhang and O. V. Prezhdo, ACS Energy Lett., 2017, 2, 1270–1278.
- 160 L. Wei, W. Ma, C. Lian and S. Meng, J. Phys. Chem. C, 2017, 121, 5905–5913.
- 161 Y. Shi, O. V. Prezhdo, J. Zhao and W. A. Saidi, ACS Energy Lett., 2020, 5, 1346–1354.
- 162 J. He and R. Long, J. Phys. Chem. Lett., 2018, 9, 6489-6495.
- 163 W. Li, Y.-Y. Sun, L. Li, Z. Zhou, J. Tang and O. V. Prezhdo, J. Am. Chem. Soc., 2018, 140, 15753–15763.
- 164 D. J. Vogel, T. M. Inerbaev and D. S. Kilin, J. Phys. Chem. C, 2018, 122, 5216–5226.
- 165 J. He, W.-H. Fang and R. Long, *Chem. Sci.*, 2019, **10**, 10079–10088.
- 166 W. Chu, W. A. Saidi, J. Zhao and O. V. Prezhdo, *Angew. Chem., Int. Ed.*, 2020, **59**, 6435–6441.
- 167 X. Zhang, M. E. Turiansky and C. G. Van de Walle, J. Phys. Chem. C, 2020, 124, 6022–6027.
- 168 B. Peng, G. Yu, Y. Zhao, Q. Xu, G. Xing, X. Liu, D. Fu, B. Liu, J. R. S. Tan, W. Tang, H. Lu, J. Xie, L. Deng, T. C. Sum and K. P. Loh, ACS Nano, 2016, 10, 6383–6391.
- 169 Z. Zhang, L. Qiao, C. Mora-Perez, R. Long and O. V. Prezhdo, J. Chem. Phys., 2020, 152, 064707.
- 170 J. Wang, W. Li and W. Yin, Adv. Mater., 2019, 32, 1906115.
- 171 L. Qiao, W.-H. Fang, R. Long and O. V. Prezhdo, *Angew. Chem., Int. Ed.*, 2020, **59**, 4684–4690.
- 172 W. Li, J. Zhan, X. Liu, J. Tang, W.-J. Yin and O. V. Prezhdo, *Chem. Mater.*, 2021, 33, 1285–1292.
- 173 L. Qiao, W.-H. Fang and R. Long, *Angew. Chem., Int. Ed.*, 2020, **59**, 13347–13353.
- 174 J. He, W.-H. Fang, R. Long and O. V. Prezhdo, *Nano Energy*, 2021, **79**, 105491.
- 175 N. Aristidou, C. Eames, I. Sanchez-Molina, X. Bu, J. Kosco, M. S. Islam and S. A. Haque, *Nat. Commun.*, 2017, 8, 15218.
- 176 A. Szemjonov, K. Galkowski, M. Anaya, Z. Andaji-Garmaroudi, T. K. Baikie, S. Mackowski, I. D. Baikie, S. D. Stranks and M. S. Islam, ACS Mater. Lett., 2019, 1, 506–510.
- 177 J. He, W.-H. Fang, R. Long and O. V. Prezhdo, *J. Am. Chem. Soc.*, 2020, **142**, 14664–14673.
- 178 L. Qiao, R. Long and W.-H. Fang, *J. Phys. Chem. Lett.*, 2019, 5499–5506.
- 179 J. He, W. Fang, R. Long and O. V. Prezhdo, *J. Am. Chem. Soc.*, 2019, **141**, 5798–5807.

180 N. Aristidou, C. Eames, I. Sanchez-Molina, X. Bu, J. Kosco, M. S. Islam and S. A. Haque, *Nat. Commun.*, 2017, 8, 15319

Nanoscale

- 181 Y. Ouyang, Y. Li, P. Zhu, Q. Li, Y. Gao, J. Tong, L. Shi, Q. Zhou, C. Ling, Q. Chen, Z. Deng, H. Tan, W. Deng and J. Wang, J. Mater. Chem. A, 2019, 7, 2275–2282.
- 182 J. He, Y. Zhu, W. Fang and R. Long, *J. Phys. Chem. Lett.*, 2021, **12**, 1664–1670.
- 183 C.-J. Tong, L. Li, L.-M. Liu and O. V. Prezhdo, *J. Am. Chem. Soc.*, 2020, **142**, 3060–3068.
- T. A. S. Doherty, A. J. Winchester, S. Macpherson,
 D. N. Johnstone, V. Pareek, E. M. Tennyson, S. Kosar,
 F. U. Kosasih, M. Anaya, M. Abdi-Jalebi, Z. Andaji-Garmaroudi, E. L. Wong, J. Madéo, Y.-H. Chiang,
 J.-S. Park, Y.-K. Jung, C. E. Petoukhoff, G. Divitini,
 M. K. L. Man, C. Ducati, A. Walsh, P. A. Midgley,
 K. M. Dani and S. D. Stranks, *Nature*, 2020, 580, 360–366.
- 185 G. W. P. Adhyaksa, S. Brittman, H. Āboliņš, A. Lof, X. Li, J. D. Keelor, Y. Luo, T. Duevski, R. M. A. Heeren, S. R. Ellis, D. P. Fenning and E. C. Garnett, *Adv. Mater.*, 2018, 30, 1804792.
- 186 R. Long, J. Liu and O. V. Prezhdo, *J. Am. Chem. Soc.*, 2016, **138**, 3884–3890.
- 187 Z. Chu, M. Yang, P. Schulz, D. Wu, X. Ma, E. Seifert, L. Sun, X. Li, K. Zhu and K. Lai, *Nat. Commun.*, 2017, 8, 2230.
- 188 W.-J. Yin, T. Shi and Y. Yan, *Adv. Mater.*, 2014, **26**, 4653-4658.
- 189 W.-J. Yin, Y. Wu, S.-H. Wei, R. Noufi, M. M. Al-Jassim and Y. Yan, *Adv. Energy Mater.*, 2014, 4, 1300712.
- 190 J. S. Yun, A. Ho-Baillie, S. Huang, S. H. Woo, Y. Heo, J. Seidel, F. Huang, Y.-B. Cheng and M. A. Green, *J. Phys. Chem. Lett.*, 2015, 6, 875–880.
- 191 L. Song, X. Guo, Y. Hu, Y. Lv, J. Lin, Y. Fan, N. Zhang and X. Liu, *Nanoscale*, 2018, 10, 18315–18322.
- 192 B. Li, Y. Zhang, L. Zhang and L. Yin, *J. Power Sources*, 2017, **360**, 11–20.
- 193 Y. Guo, Q. Wang and W. A. Saidi, *J. Phys. Chem. C*, 2017, 121, 1715–1722.
- 194 Y. Wang, W.-H. Fang, R. Long and O. V. Prezhdo, *J. Phys. Chem. Lett.*, 2019, **10**, 1617–1623.
- 195 Y. Wang, J. He, Y. Yang, Z. Zhang and R. Long, *ACS Appl. Energy Mater.*, 2019, 2, 3419–3426.
- 196 J.-S. Park and A. Walsh, *Annu. Rev. Condens. Matter Phys.*, 2021, **12**, 95–109.
- 197 L. Qiao, W.-H. Fang, R. Long and O. V. Prezhdo, *ACS Energy Lett.*, 2020, 3813–3820.
- 198 G. Xing, B. Wu, X. Wu, M. Li, B. Du, Q. Wei, J. Guo, E. K. L. Yeow, T. C. Sum and W. Huang, *Nat. Commun.*, 2017, 8, 14558.
- 199 Z. Xiao, W. Meng, B. Saparov, H.-S. Duan, C. Wang, C. Feng, W. Liao, W. Ke, D. Zhao, J. Wang, D. B. Mitzi and Y. Yan, *J. Phys. Chem. Lett.*, 2016, 7, 1213–1218.
- 200 L. Gan, J. Li, Z. Fang, H. He and Z. Ye, *J. Phys. Chem. Lett.*, 2017, **8**, 5177–5183.
- 201 N. Liu, P. Liu, H. Zhou, Y. Bai and Q. Chen, *J. Phys. Chem. Lett.*, 2020, 11, 3521–3528.

- 202 A. Fraccarollo, V. Cantatore, G. Boschetto, L. Marchese and M. Cossi, *J. Chem. Phys.*, 2016, **144**, 164701.
- 203 D. Wang, B. Wen, Y.-N. Zhu, C.-J. Tong, Z.-K. Tang and L.-M. Liu, J. Phys. Chem. Lett., 2017, 8, 876–883.
- 204 D. Ghosh, D. Acharya, L. Pedesseau, C. Katan, J. Even, S. Tretiak and A. J. Neukirch, *J. Mater. Chem. A*, 2020, 8, 22009–22022.
- 205 S.-F. Zhang, X.-K. Chen, A.-M. Ren, H. Li and J.-L. Bredas, ACS Energy Lett., 2019, 4, 17–25.
- 206 Y.-T. Li, L. Ding, J.-Z. Li, J. Kang, D.-H. Li, L. Ren, Z.-Y. Ju, M.-X. Sun, J.-Q. Ma, Y. Tian, G.-Y. Gou, D. Xie, H. Tian, Y. Yang, L.-W. Wang, L.-M. Peng and T.-L. Ren, ACS Cent. Sci., 2019, 5, 1857–1865.
- 207 V. A. Hintermayr, L. Polavarapu, A. S. Urban and J. Feldmann, ACS Nano, 2018, 12, 10151–10158.
- 208 J. Yin, P. Maity, R. Naphade, B. Cheng, J.-H. He, O. M. Bakr, J.-L. Brédas and O. F. Mohammed, *ACS Nano*, 2019, 13, 12621–12629.
- 209 Z. Zhang, W.-H. Fang, M. V. Tokina, R. Long and O. V. Prezhdo, *Nano Lett.*, 2018, 18, 2459–2466.
- 210 J. He, W.-H. Fang and R. Long, J. Phys. Chem. Lett., 2020, 11, 5100–5107.
- 211 J.-C. Blancon, H. Tsai, W. Nie, C. C. Stoumpos, L. Pedesseau, C. Katan, M. Kepenekian, C. M. M. Soe, K. Appavoo, M. Y. Sfeir, S. Tretiak, P. M. Ajayan, M. G. Kanatzidis, J. Even, J. J. Crochet and A. D. Mohite, Science, 2017, 355, 1288–1292.
- 212 Z. Zhang, K. Yu and G. Wang, *Adv. Electron. Mater.*, 2019, 5, 1900216.
- 213 Z. Zhang, W.-H. Fang, R. Long and O. V. Prezhdo, *J. Am. Chem. Soc.*, 2019, **141**, 15557–15566.
- 214 A. Preske, S. W. O'Neill, B. D. Swartz, J. Liu, O. V. Prezhdo and T. D. Krauss, *Chem. Mater.*, 2019, **31**, 8301–8307.
- 215 R. Shi, A. S. Vasenko, R. Long and O. V. Prezhdo, *J. Phys. Chem. Lett.*, 2020, **11**, 9100–9109.
- 216 G. J. Hedley, C. Quarti, J. Harwell, O. V. Prezhdo, D. Beljonne and I. D. W. Samuel, *Sci. Rep.*, 2018, **8**, 8115.
- 217 A. Solanki, P. Yadav, S.-H. Turren-Cruz, S. S. Lim, M. Saliba and T. C. Sum, *Nano Energy*, 2019, 58, 604–611.
- 218 H. Kawai, G. Giorgi, A. Marini and K. Yamashita, *Nano Lett.*, 2015, 15, 3103–3108.
- 219 Y. Yang, D. P. Ostrowski, R. M. France, K. Zhu, J. van de Lagemaat, J. M. Luther and M. C. Beard, *Nat. Photonics*, 2016, 10, 53–59.
- 220 H. Shi, X. Zhang, X. Sun and X. Zhang, *Appl. Phys. Lett.*, 2020, **116**, 151902.
- 221 X. Jia, J. Jiang, Y. Zhang, J. Qiu, S. Wang, Z. Chen, N. Yuan and J. Ding, *Appl. Phys. Lett.*, 2018, **112**, 143903.
- 222 J. Yang, X. Wen, H. Xia, R. Sheng, Q. Ma, J. Kim, P. Tapping, T. Harada, T. W. Kee, F. Huang, Y.-B. Cheng, M. Green, A. Ho-Baillie, S. Huang, S. Shrestha, R. Patterson and G. Conibeer, *Nat. Commun.*, 2017, 8, 14120.
- 223 P. P. Joshi, S. F. Maehrlein and X. Zhu, *Adv. Mater.*, 2019, **31**, 1803054.
- 224 A. C. Ferreira, A. Létoublon, S. Paofai, S. Raymond, C. Ecolivet, B. Rufflé, S. Cordier, C. Katan,

Review

M. I. Saidaminov, A. A. Zhumekenov, O. M. Bakr, J. Even

225 J. Fu, Q. Xu, G. Han, B. Wu, C. H. A. Huan, M. L. Leek and T. C. Sum, *Nat. Commun.*, 2017, **8**, 1300.

and P. Bourges, Phys. Rev. Lett., 2018, 121, 085502.

226 T. R. Hopper, A. Gorodetsky, A. Jeong, F. Krieg,
M. I. Bodnarchuk, M. Maimaris, M. Chaplain,
T. J. Macdonald, X. Huang, R. Lovrincic, M. V. Kovalenko

and A. A. Bakulin, Nano Lett., 2020, 20, 2271-2278.

- 227 M. E.-A. Madjet, A. V. Akimov, F. El-Mellouhi, G. R. Berdiyorov, S. Ashhab, N. Tabet and S. Kais, *Phys. Chem. Chem. Phys.*, 2016, **18**, 5219–5231.
- 228 M. E. Madjet, G. R. Berdiyorov, F. El-Mellouhi, F. H. Alharbi, A. V. Akimov and S. Kais, *J. Phys. Chem. Lett.*, 2017, 8, 4439–4445.
- 229 D. Meggiolaro, E. Mosconi and F. De Angelis, *ACS Energy Lett.*, 2018, 3, 447–451.
- 230 S. Banerjee, J. Kang, X. Zhang and L.-W. Wang, *J. Chem. Phys.*, 2020, **152**, 091102.
- 231 H. Zhu, K. Miyata, Y. Fu, J. Wang, P. P. Joshi, D. Niesner, K. W. Williams, S. Jin and X. Y. Zhu, *Science*, 2016, 353, 1409–1413.
- 232 Z. Zhang, R. Long, M. V. Tokina and O. V. Prezhdo, J. Am. Chem. Soc., 2017, 139, 17327–17333.
- 233 S. Kaniyankandy and S. Neogy, *J. Photochem. Photobiol., A*, 2020, **401**, 112761.
- 234 Q. Shen, T. S. Ripolles, J. Even, Y. Ogomi, K. Nishinaka, T. Izuishi, N. Nakazawa, Y. Zhang, C. Ding, F. Liu, T. Toyoda, K. Yoshino, T. Minemoto, K. Katayama and S. Hayase, *Appl. Phys. Lett.*, 2017, 111, 153903.
- 235 D. J. Vogel, A. Kryjevski, T. M. Inerbaev and D. S. Kilin, J. Phys. Chem. Lett., 2017, 8, 3032–3039.
- 236 W. Li, L. Zhou, O. V. Prezhdo and A. V. Akimov, *ACS Energy Lett.*, 2018, 3, 2159–2166.
- 237 X.-Y. Liu, J.-J. Yang, W.-K. Chen, A. V. Akimov, W.-H. Fang and G. Cui, *J. Phys. Chem. Lett.*, 2021, 1131–1137.
- 238 B. Smith, M. Shakiba and A. V. Akimov, *J. Phys. Chem. Lett.*, 2021, 2444–2453.
- 239 R. Franklin-Mergarejo, D. O. Alvarez, S. Tretiak and S. Fernandez-Alberti, *Sci. Rep.*, 2016, **6**, 31253.
- 240 K. Hyeon-Deuk and O. V. Prezhdo, ACS Nano, 2012, 6, 1239–1250.
- 241 K. Hyeon-Deuk and O. V. Prezhdo, *Nano Lett.*, 2011, **11**, 1845–1850.
- 242 S. Kim, S. Hood, J. Park, L. Whalley and A. Walsh, *J. Phys. Energy*, 2020, 2, 036001.
- 243 F. Zheng and L. Wang, Energy Environ. Sci., 2019, 12, 1219–1230.
- 244 D. A. Hoff, R. da Silva and L. G. C. Rego, *J. Phys. Chem. C*, 2012, **116**, 21169–21178.
- 245 D. A. Hoff and L. G. C. Rego, in *Chemical Modelling*, ed. M. Springborg and J.-O. Joswig, Royal Society of Chemistry, Cambridge, 2013, vol. 10, pp. 102–126.
- 246 W. Jiang, D. J. Hardy, J. C. Phillips, A. D. MacKerell, K. Schulten and B. Roux, *J. Phys. Chem. Lett.*, 2011, 2, 87–92.
- 247 H. Chen, H. Fu, X. Shao, C. Chipot and W. Cai, *J. Chem. Inf. Model.*, 2018, **58**, 1315–1318.

- 248 A. Monti, C. F. A. Negre, V. S. Batista, L. G. C. Rego, H. J. M. de Groot and F. Buda, *J. Phys. Chem. Lett.*, 2015, 6, 2393–2398.
- 249 L. G. C. Rego and V. S. Batista, *J. Am. Chem. Soc.*, 2003, 125, 7989–7997.
- 250 S. Pal, D. J. Trivedi, A. V. Akimov, B. Aradi, T. Frauenheim and O. V. Prezhdo, J. Chem. Theory Comput., 2016, 12, 1436–1448.
- 251 A. V. Akimov, J. Chem. Theory Comput., 2016, 12, 5719–5736.
- 252 H. Uratani and H. Nakai, J. Phys. Chem. Lett., 2020, 11, 4448-4455.
- 253 S. S. R. K. C. Yamijala and P. Huo, *J. Phys. Chem. A*, 2021, **125**, 628–635.
- 254 H. Uratani and H. Nakai, J. Chem. Phys., 2020, 152, 224109.
- 255 D. G. Fedorov, T. Ishida and K. Kitaura, J. Phys. Chem. A, 2005, 109, 2638–2646.
- 256 H. Oberhofer and J. Blumberger, *J. Chem. Phys.*, 2010, **133**, 244105.
- 257 B. Nebgen and O. V. Prezhdo, *J. Phys. Chem. A*, 2016, **120**, 7205–7212.
- 258 B. Smith and A. V. Akimov, *J. Phys. Chem. Lett.*, 2020, 11, 1456–1465.
- 259 A. V. Akimov, J. Phys. Chem. Lett., 2017, 8, 5190-5195.
- 260 P. O. Dral, J. Phys. Chem. Lett., 2020, 11, 2336-2347.
- 261 D. Hu, Y. Xie, X. Li, L. Li and Z. Lan, *J. Phys. Chem. Lett.*, 2018, **9**, 2725–2732.
- 262 P. O. Dral, in Advances in Quantum Chemistry, ed. K. Ruud and E. J. Brändas, Academic Press, 2020, vol. 81, pp. 291–324.
- 263 P. O. Dral, M. Barbatti and W. Thiel, J. Phys. Chem. Lett., 2018, 9, 5660–5663.
- 264 W.-K. Chen, X.-Y. Liu, W.-H. Fang, P. O. Dral and G. Cui, *J. Phys. Chem. Lett.*, 2018, **9**, 6702–6708.
- 265 J.-K. Ha, K. Kim and S. K. Min, *J. Chem. Theory Comput.*, 2021, 17, 694–702.
- 266 V. Gladkikh, D. Y. Kim, A. Hajibabaei, A. Jana, C. W. Myung and K. S. Kim, *J. Phys. Chem. C*, 2020, **124**, 8905–8918.
- 267 Z. Zhang, Y. Zhang, J. Wang, J. Xu and R. Long, *J. Phys. Chem. Lett.*, 2021, 10572–10579.
- 268 V. Polo, E. Kraka and D. Cremer, Mol. Phys., 2002, 100, 1771–1790.
- 269 J. Heyd, G. E. Scuseria and M. Ernzerhof, J. Chem. Phys., 2003, 118, 8207–8215.
- 270 W. Chen and A. Pasquarello, *Phys. Rev. B: Condens. Matter Mater. Phys.*, 2015, **92**, 041115.
- 271 R. J. Hunt, M. Szyniszewski, G. I. Prayogo, R. Maezono and N. D. Drummond, *Phys. Rev. B*, 2018, **98**, 075122.
- 272 M. P. Esch, Y. Shu and B. G. Levine, J. Phys. Chem. A, 2019, 123, 2661–2673.
- 273 J. Even, L. Pedesseau, J.-M. Jancu and C. Katan, *J. Phys. Chem. Lett.*, 2013, **4**, 2999–3005.
- 274 D. Meggiolaro and F. De Angelis, *ACS Energy Lett.*, 2018, 3, 2206–2222.

275 D. A. Egger and L. Kronik, *J. Phys. Chem. Lett.*, 2014, 5, 2728–2733.

Nanoscale

- 276 Y. Lin and A. V. Akimov, J. Phys. Chem. A, 2016, 120, 9028–9041.
- 277 L. Li, J. C. Wong and Y. Kanai, J. Chem. Theory Comput., 2017, 13, 2634–2641.
- 278 Z. Zhou, J. Liu, R. Long, L. Li, L. Guo and O. V. Prezhdo, *J. Am. Chem. Soc.*, 2017, **139**, 6707–6717.
- 279 G. E. Eperon, E. Jedlicka and D. S. Ginger, J. Phys. Chem. Lett., 2018, 9, 104–109.
- 280 F. Staub, U. Rau and T. Kirchartz, ACS Omega, 2018, 3, 8009–8016.
- 281 X. Hou, J. Kang, H. Qin, X. Chen, J. Ma, J. Zhou, L. Chen, L. Wang, L.-W. Wang and X. Peng, *Nat. Commun.*, 2019, 10, 1750.
- 282 Y. Li, T. Ding, X. Luo, Z. Chen, X. Liu, X. Lu and K. Wu, *Nano Res.*, 2019, **12**, 619–623.
- 283 X. Zhang, J.-X. Shen and C. G. V. de Walle, *Adv. Energy Mater.*, 2020, **10**, 1902830.

- 284 J.-X. Shen, X. Zhang, S. Das, E. Kioupakis and C. G. V. de Walle, *Adv. Energy Mater.*, 2018, **8**, 1801027.
- 285 L. Li, M.-F. Lin, X. Zhang, A. Britz, A. Krishnamoorthy, R. Ma, R. K. Kalia, A. Nakano, P. Vashishta, P. Ajayan, M. C. Hoffmann, D. M. Fritz, U. Bergmann and O. V. Prezhdo, *Nano Lett.*, 2019, 19, 6078–6086.
- 286 E. Pradhan, K. Sato and A. V. Akimov, *J. Phys.: Condens. Matter*, 2018, **30**, 484002.
- 287 H. Zhu, Y. Yang, K. Hyeon-Deuk, M. Califano, N. Song, Y. Wang, W. Zhang, O. V. Prezhdo and T. Lian, *Nano Lett.*, 2014, 14, 1263–1269.
- 288 K. Hyeon-Deuk, J. Kim and O. V. Prezhdo, *J. Phys. Chem. Lett.*, 2015, **6**, 244–249.
- 289 D. J. Trivedi, L. Wang and O. V. Prezhdo, *Nano Lett.*, 2015, 15, 2086–2091.
- 290 G. Zhou, G. Lu and O. V. Prezhdo, *Nano Lett.*, 2020, 21, 756–761.
- 291 X. Jiang, Q. Zheng, Z. Lan, W. A. Saidi, X. Ren and J. Zhao, *Sci. Adv.*, 2021, 7, eabf3759.